nanomaterials

MDPI

Article

Carbon-Supported Trimetallic Catalysts (PdAuNi/C) for Borohydride Oxidation Reaction

Ahmed M. A. ElSheikh [1,2,†], Gordana Backović [3,†], Raisa C. P. Oliveira [3], César A. C. Sequeira [3], James McGregor [2], Biljana Šljukić [3] and Diogo M. F. Santos [3,*]

1 Mechanical Engineering Department, South Valley University, AlShobaan AlMoslemeen Street, Qena 83521, Egypt; ahmed.elsheikh@eng.svu.edu.eg
2 Department of Chemical and Biological Engineering, University of Sheffield, Sheffield S1 3JD, UK; james.mcgregor@sheffield.ac.uk
3 Center of Physics and Engineering of Advanced Materials (CeFEMA), Instituto Superior Técnico, Universidade de Lisboa, 1049-001 Lisboa, Portugal; gordanabackovic@tecnico.ulisboa.pt (G.B.); raisa.oliveira@tecnico.ulisboa.pt (R.C.P.O.); cesarsequeira@tecnico.ulisboa.pt (C.A.C.S.); biljana.paunkovic@tecnico.ulisboa.pt (B.Š.)
* Correspondence: diogosantos@tecnico.ulisboa.pt; Tel.: +351-218417765
† Equally contributed.

Abstract: The synthesis of palladium-based trimetallic catalysts via a facile and scalable synthesis procedure was shown to yield highly promising materials for borohydride-based fuel cells, which are attractive for use in compact environments. This, thereby, provides a route to more environmentally friendly energy storage and generation systems. Carbon-supported trimetallic catalysts were herein prepared by three different routes: using a $NaBH_4$-ethylene glycol complex (PdAuNi/C_{SBEG}), a $NaBH_4$-2-propanol complex (PdAuNi/C_{SBIPA}), and a three-step route (PdAuNi/$C_{3\text{-step}}$). Notably, PdAuNi/C_{SBIPA} yielded highly dispersed trimetallic alloy particles, as determined by XRD, EDX, ICP-OES, XPS, and TEM. The activity of the catalysts for borohydride oxidation reaction was assessed by cyclic voltammetry and RDE-based procedures, with results referenced to a Pd/C catalyst. A number of exchanged electrons close to eight was obtained for PdAuNi/$C_{3\text{-step}}$ and PdAuNi/C_{SBIPA} (7.4 and 7.1, respectively), while the others, PdAuNi/C_{SBEG} and Pd/C_{SBIPA}, presented lower values, 2.8 and 1.2, respectively. A direct borohydride-peroxide fuel cell employing PdAuNi/C_{SBIPA} catalyst in the anode attained a power density of 47.5 mW cm^{-2} at room temperature, while the elevation of temperature to 75 °C led to an approximately four-fold increase in power density to 175 mW cm^{-2}. Trimetallic catalysts prepared via this synthesis route have significant potential for future development.

Keywords: palladium; trimetallic catalysts; nanoparticle; borohydride oxidation; direct borohydride peroxide fuel cell; kinetic parameters

Citation: ElSheikh, A.M.A.; Backović, G.; Oliveira, R.C.P.; Sequeira, C.A.C.; McGregor, J.; Šljukić, B.; Santos, D.M.F. Carbon-Supported Trimetallic Catalysts (PdAuNi/C) for Borohydride Oxidation Reaction. *Nanomaterials* **2021**, *11*, 1441. https://doi.org/10.3390/nano11061441

Academic Editor: Stefano Agnoli

Received: 4 May 2021
Accepted: 24 May 2021
Published: 29 May 2021

1. Introduction

Fuel cells (FCs) are electrochemical energy conversion devices with superior performance compared to conventional internal combustion engines, as they are not limited by the Carnot cycle [1]. Additionally, FCs are more environmentally friendly than conventional energy generation processes since they generally do not generate carbon dioxide (with few exceptions, such as direct alcohol/formic acid FCs) and do not rely on the consumption of fossil resources. Consequently, FC research and development has grown linearly with the worldwide energy demand and is projected to increase as FCs replace conventional heat engines in various applications [2]. However, many challenges need to be overcome if mass uptake of fuel cells is to be realized, including issues of safety, fuel source, and ensuring high efficiencies at low operating temperatures.

Low-temperature FCs targeted for use in portable applications and, particularly, for use in the transportation area have recently undergone rapid development [3]. They are

compact, lightweight, and can attain high power densities. Polymer electrolyte membrane fuel cell (PEMFC), the most developed FC, most commonly comprises an H_2-supplied anode and an O_2-supplied cathode separated by a polymeric membrane. Nevertheless, employing H_2 as fuel presents several challenges to widespread adoption, including safety, storage, and supply. Furthermore, H_2-stream pretreatment is usually required in order to remove trace carbon monoxide, which poisons the electrode. To address these issues, H_2/O_2 PEMFCs can be replaced with direct liquid fuel cells (DLFCs). DLFCs can use organic and inorganic liquid fuels, which usually incorporate a supporting electrolyte in their composition [4].

Solutions of complex hydrides (e.g., $LiBH_4$, $NaBH_4$, or KBH_4) are examples of hydrogen-containing compounds that can be used as fuels in DLFCs. Sodium borohydride ($NaBH_4$) presents many advantages over other fuels. The open-circuit voltage (OCV) for the direct borohydride fuel cell (DBFC, 1.64 V) is higher than that of the direct methanol fuel cell (DMFC, 1.21 V) and the H_2/O_2 PEMFC (1.23 V). While the oxidation of H_2 and methanol generates two and six electrons, respectively, per molecule, BH_4^- direct oxidation generates eight electrons. Consequently, DBFC possesses specific energy over 50% higher than that of the DMFC [5]. Indig and Snyder [6] demonstrated in the 1960s that electricity could be produced via anodic oxidation of borohydride and O_2 cathodic reduction, as shown in Equation (1) and Equation (2), respectively, to yield the overall fuel cell reaction (Equation (3)), where SHE stands for standard hydrogen electrode.

$$\text{BOR} \quad NaBH_4 + 8\,OH^- \rightarrow NaBO_2 + 6\,H_2O + 8\,e^- \qquad E^0 = -1.24 \text{ vs. SHE} \tag{1}$$

$$\text{ORR} \quad 2\,O_2 + 4\,H_2O + 8\,e^- \rightarrow 8\,OH^- \qquad E^0 = 0.40 \text{ vs. SHE} \tag{2}$$

$$\text{Overall} \quad NaBH_4 + 2\,O_2 \rightarrow NaBO_2 + 2\,H_2O \qquad E_0 = 1.64 \text{ V} \tag{3}$$

Many authors have discussed the advantages, disadvantages, and state-of-the-art in DBFCs, including postulating the replacement of O_2 by hydrogen peroxide (H_2O_2) [7–10]. The use of H_2O_2 as an oxidant has become more popular in recent years, in particular as this results in an entirely liquid FC, thereby facilitating its use in applications where a compact design is required. When H_2O_2 is used as the oxidant, the catholyte consists of an acidic solution of H_2O_2 in order to avoid its decomposition into H_2O and O_2. Consequently, the DBFC in which the hydrogen peroxide reduction reaction (HPRR) takes place at the cathode and the BOR at the anode is known as the direct borohydride-peroxide fuel cell (DBPFC). It can generate electricity through Equations (1) and (4), with Equation (5) being the overall FC reaction.

$$\text{HPRR} \quad H_2O_2 + 2e^- + 2H^+ \rightarrow 2\,H_2O \qquad E^0 = 1.78 \text{ V vs. SHE} \tag{4}$$

$$\text{Overall} \quad NaBH_4 + 4H_2O_2 \rightarrow NaBO_2 + 6H_2O \qquad E^0 = 3.01 \text{ V vs. SHE} \tag{5}$$

The majority of published research on DBFCs discusses the need for effective and low-cost anode and cathode materials in order to facilitate the commercialization of DBFCs. This is a result of the high operating costs of the DBFC, which is correlated with the performance, efficiency, and cost of the electrocatalysts [5,8–11]. In fact, anodic catalysts for DBFCs must have high catalytic activity for BOR and be inert towards BH_4^- hydrolysis, a chemical side reaction where BH_4^- is consumed, generating H_2 and BO_2^-. In addition, DBFC anodes need to exhibit chemical stability in a basic solution. Common anodic catalysts for DBFCs include noble metal catalysts such as Au [12–16], Pt [17–20], and their corresponding alloy materials [21–24], as well as some nonprecious metal catalysts, e.g., Ni [25,26], Zn [27], and Co [28–30]. In particular, Au has been extensively studied, as it was originally thought to be capable of inhibiting borohydride hydrolysis; however, it exhibits rather slow kinetics for borohydride oxidation [31,32]. Studies involving Au, Pd, and Pt bulk electrodes for BOR revealed that surface poisoning by reaction intermediates, including BH_{ads} or BH_3, was significantly different for the three noble metals. Results have shown that this effect was more severe for Pt and also that the Au surface was the

least affected by poisoning [33]. Despite this observation, Pt-based catalysts typically demonstrate faster electrode kinetics in BOR [24,34,35]; however, limited resources hinder their application as DBFC anodic catalysts. Pd is a promising alternative to Pt, presenting similar chemical properties and reactivity. Pd is considerably more abundant in the Earth's crust than Pt (ca. fifty times) and hence presents fewer challenges regarding resource scarcity [36–38]. Therefore, Pd has been tested in FCs both as a cocatalyst with Pt and as a Pt-free catalyst [37,39–41]. Decreasing the required quantity of Pd by mixing it with non-noble metals in a well-designed catalytic structure capable of efficient borohydride oxidation can decrease the cost of membrane electrode assemblies (MEAs) and boost the commercialization of DBFCs. It was previously found that co-doping can improve the catalytic performance of noble metal catalysts [42–44]. For example, a Pd-Co/C nanocatalyst has been demonstrated as an electrocatalyst for formic acid oxidation and methanol oxidation [45,46].

Previous studies reported Pd nanocatalysts and Pd nanoalloys as anodic catalysts for BOR in DBFCs [47,48]. Furthermore, Simões et al. [49] analyzed how Pd, Au, and Pd-Au carbon-supported nanoparticles with different compositions performed during BOR in alkaline media. Pd_xAu_{1-x}/C electrocatalyst exhibited an open circuit potential (OCP) lower than Pd and Au did. Merino-Jimenez et al. [50] evaluated a titanium-supported and carbon nanofiber-covered Pd-Ir alloy for BOR. The authors concluded that alloying Pd with Ir improves Pd electroactivity towards BOR. This enhancement was associated with the favoring of BOR (direct oxidation) and suppression of hydrogen evolution reaction (HER). Furthermore, Grimmer et al. [51] studied BOR at Pd/C by cyclic voltammetry, rotating disc electrode (RDE) measurements, chronoamperometry coupled to NMR spectrometry, and in situ Fourier transform infrared spectroscopy (FTIR). RDE results yielded n = 4 (at 0.4 V vs. reversible hydrogen electrode (RHE)) and n = 8 (at 0.8 V vs. RHE). Thus, at 0.8 V vs. RHE, BOR is 100% direct, while at 0.4 V, two different pathways are proposed to operate: (i) the total oxidation of BH_4^- to BO_2^- and two H_2 molecules and (ii) a four-electron electrooxidation with the production of BH_2^- species. The authors also suggested that at low potentials, Pd-BH_2OH species block surface sites, while at higher potentials, this intermediate is fully oxidized (n = 8). Additionally, Pd has been shown to be relatively unharmed by surface poisoning, preserving good BOR kinetics even in highly concentrated BH_4^- solutions relevant for DBPFC operation [33]. Recently, by screening selected metal combinations (e.g., Pd with Co, Au, Ti) over a wide range of compositions, bimetallic and trimetallic Pd-based materials with optimum compositions that exhibited good activity for BOR were identified [51–56]. According to multiple published reports, Ni presents several benefits when added as a cocatalyst to C-supported Pd. First, it is an Earth-abundant metal, and therefore its use tackles issues of resource scarcity and reduces cost. Secondly, it is oxyphilic and capable of generating the oxygen species necessary for the redox reaction. Finally, the presence of Ni can exert an electronic effect over Pd, altering and potentially enhancing the catalytic properties of the latter [57–59].

In this work, investigations on the oxidation of BH_4^- in alkaline media at different working conditions are presented for a selection of trimetallic carbon-supported catalysts based on Pd (PdAuNi/C), prepared by a facile and scalable synthetic route. There is a consensus that adding a second metal as a cocatalyst to Pd is beneficial for its electrocatalytic performance. This is due to the electronic, geometric, and bifunctional effects that the second metal can provide. Previous works have considered multiplying the catalytic benefits by adding two metals to Pd instead of one [56,60–66]. It is hypothesized that adding two metals, such as Au and Ni, each of which is known to be a beneficial addition to Pd individually [67–69], would significantly enhance Pd electrocatalytic performance. A small number of previous studies have previously investigated PdAuNi electrocatalysts [67–72]. Au [12,73–77] and Ni [25,78–80], like Pd, have been proven to possess good catalytic activity towards BOR, which makes their incorporation in a catalyst additionally attractive. Specifically, in the case of Ni electrodes, the formation of β-NiOOH has been pointed out as essential for the oxidation of BH_4^- [26]. Furthermore, to maximize the potential for

BOR, a high-surface inert, mesoporous, and conductive support material is necessary to anchor the trimetallic nanoparticles and prevent their coalescence. Vulcan carbon (XC-72R) is commonly applied for this application due to its high surface area, mesoporous structure, and affordable cost. It was therefore chosen to support the PdAuNi and Pd nanoparticles. There are various chemical and physical synthetic routes in the literature to prepare dispersed metal nanoparticles [81]. The synthesis protocol is thought to play a crucial role and contribute to the catalyst physicochemical and catalytic characteristics. Any chosen method should balance between fine-tuned catalytic properties and ease of preparation, leading potentially to facile mass production [82]. $NaBH_4$ metal reduction is a very common means to prepare C-supported catalysts due to its easy procedure and quality-produced catalysts. Moreover, there is more than one $NaBH_4$ protocol to prepare Pd-supported nanoparticles. This work aims to synthesize three carbon-based trimetallic catalysts based on different borohydride reduction protocols. The physicochemical and morphological properties of those materials were determined and compared. Their performance as electrocatalysts for BOR was analyzed and discussed considering the different synthesis routes employed and the final properties obtained for each material.

2. Materials and Methods

2.1. Chemicals

Metallic precursors ($PdCl_2$, $NiCl_2$, and $AuCl_3$) to synthesize PdAuNi/C electrocatalysts were purchased from Sigma-Aldrich (St. Louis, MO, USA). Vulcan carbon (XC-72R), purchased from Cabot Corp (Boston, MA, USA), was used to support the synthesized metal nanoparticles. $NaBH_4$ (SB, 96 wt.%), ethylene glycol (EG, 99.5 wt.%), 2-propanol (IPA, 99 wt.%), NaOH (85 wt.%), and ethanol (100%) were purchased from Sigma-Aldrich. For the electrochemical measurements, $NaBH_4$ (98 wt.%, Scharlau, Barcelona, Spain) and H_2O_2 (30 vol.%, Carlo Erba, Barcelona, Spain) were used. All chemicals were used as received without further purification.

2.2. Catalyst Preparation

Three borohydride reduction protocols using (i) a $NaBH_4$-ethylene glycol complex, (ii) a $NaBH_4$-2-propanol complex, and (iii) a three-step route were deployed to synthesize carbon-supported PdAuNi catalysts denoted herein as PdAuNi/C_{SBEG}, PdAuNi/C_{SBIPA}, and PdAuNi/$C_{3\text{-step}}$, respectively. The theoretical metal loading based on the quantity of metal salts used in the synthesis was 12 wt.% for PdAuNi/C_{SBIPA} and 20 wt.% for both PdAuNi/C_{SBEG} and PdAuNi/$C_{3\text{-step}}$. Although electrocatalysts for laboratory studies usually load the carbon support with 20 to 40 wt.% of metal, the use of lower loadings is more representative of industrial catalyst loadings which are typically ~5 wt.% [83].

The SBEG synthesis protocol uses a $NaBH_4$-ethylene glycol complex, following previous work [36,84,85]. Vulcan carbon (202 mg) was first dispersed in ethylene glycol (10 mL). The metallic precursor solution containing $PdCl_2$ (28 mg mL^{-1}), $AuCl_3$ (55 mg mL^{-1}), and $NiCl_2$ (36.7 mg mL^{-1}) was then suspended in ethylene glycol (10 mL). The two suspensions were subsequently mixed. Next, a solution of $NaBH_4$ (20 mL) was slowly added to the metal and carbon mixture under magnetic stirring. The mixture was heated to 35 °C and kept at that temperature for 3.5 h. The mixture was then left to cool and washed copiously with deionized water until neutralization. Following this, it was dried in a vacuum oven at 80 °C for 2 h.

The second reduction protocol (SBIPA) applied $NaBH_4$ following methods described in previous reports [86–89]. The Vulcan carbon and metal precursors were sonicated in a mixture of 2-propanol/water (50 vol.%). KBr was added to stabilize the metal nanoparticles. The mechanism of this is that the larger Br^- ions substitute for Cl^- ions in solution, stabilizing Pd particles and preventing further particle agglomeration [90]. Unlike an organic surfactant such as PVP, KBr can be washed off easily after synthesis from the particle surface. The KBr/metal atomic ratio was 1.5. The mixture was stirred for 10 min, followed by the addition of $NaBH_4$ solution (0.5 M, 15 mL). Stirring then continued for

another 30 min. Following this, the sample was washed under vacuum filtration. Finally, the wet powder was dried at 80 °C in a vacuum oven overnight.

The third protocol to prepare PdAuNi/C (three-step) aimed to compare the stepwise reduction of metals on the carbon surface to the co-reduction procedure practiced in the first two protocols. Consecutive reduction of different metals can lead to the formation of core@shell structures, such as Ru@Pd/C [91], Au@Pd [92,93], and Cu@Pd [94]. The $NaBH_4$-2-propanol reduction mixture was once more used to prepare this catalyst. The procedure started with sonicating Vulcan carbon (202.4 mg) in a mixture of 2-propanol/water (50 vol.%). Then, $NiCl_2$ was added and kept in the solution under stirring for 1 h. This was longer than the reduction time required for Au and Pd reduction time, as Ni is more oxyphilic and less reducible [95,96]. Subsequently, $AuCl_3$ was added with stirring for 30 min. Finally, $PdCl_2$ was added with stirring for 30 min. To illustrate the impact of adding both Au and Ni onto Pd, a monometallic C-supported Pd catalyst (Pd/C_{SBIPA}) was synthesized using the SBIPA procedure.

2.3. Physical Characterization

The crystal structure of the prepared catalysts was investigated using X-ray diffraction (XRD) with a Bruker D2 Phaser operating using Cu K_α radiation at 30 kV, 10 mA, and 12° min^{-1} scan rate. To evaluate the crystallite size, the Scherrer equation was applied using the Pd (111) peak details. To quantify the metallic species in each catalyst powder, inductively coupled plasma optical emission spectrometry (ICP-OES) was applied using a Spectro Ciros Vision spectrometer by Spectro Analytical Instruments Inc. (Kleve, Germany). The samples were first digested in HNO_3 (2%), followed by 10-fold dilution in aqua-regia (8%). The surface-weighted chemical composition of the catalysts was examined through energy-dispersive X-ray spectroscopy (EDX) attached to a JEOL JSM 6010LA scanning electron microscope (SEM) by JEOL Ltd. (Tokyo, Japan). Each catalyst surface was examined twice applying two different accelerating voltages: 10 kV and 20 kV [97] enabling studying the composition at two different depths. The catalyst morphology was examined by transmission electron microscopy (TEM) employing a Phillips C100 microscope (Hillsboro, OR, USA) operating at 100 kV applying LaB_6 filament. The TEM samples were prepared by suspending 5 mg of each sample powder in 2 mL of ethanol. Then, the mixture was sonicated for 1 h. A spray atomizer was then used to take 10 µL of the suspension to paint the holey carbon-coated Cu grid. The grid was left to dry for 24 h. The surface chemistry of the prepared electrocatalysts was studied by X-ray photoelectron spectroscopy (XPS) employing a Thermo Scientific K-Alpha+ spectrometer (Waltham, MA, USA). An Al-X ray source (72 W) and 400-μm^2 were applied. The pass energy to record the data was 150 eV for survey scans and 40 eV for high-resolution ones. The survey scan step size was 1 eV, but that of the high-resolution was 0.1 eV. Low-energy electrons and argon ions were used to neutralize the charge. CasaXPS from Casa Software Ltd. (Teignmouth, UK) was used to analyze the data and employed a Shirley-type background and Scofield cross-sections with an energy dependence of −0.6.

2.4. Working Electrode Preparation

Catalytic inks were prepared by ultrasonically dispersing 5 mg of each catalyst in 2 mL of ethanol and 25 µL of 5 wt.% Nafion suspension for 30 min. Subsequently, 5 µL of the prepared ink was deposited onto a glassy carbon electrode (GC, A = 0.0707 cm^2, inactive for BOR [98]) and left to dry at room temperature for 1 h. Catalyst loading was 0.175 mg cm^{-2} for all catalysts. The total metal loadings (calculated based on the ICP-OES results) were 0.021, 0.027, 0.039, and 0.015 mg cm^{-2} for Pd/C_{SBIPA}, $PdAuNi/C_{SBEG}$, $PdAuNi/C_{3\text{-step}}$ and $PdAuNi/C_{SBIPA}$, respectively. Pd loadings were 2.51, 2.41, 4.77, and 5.77 µg cm^{-2} for Pd/C_{SBIPA}, $PdAuNi/C_{SBEG}$, $PdAuNi/C_{3\text{-step}}$, and $PdAuNi/C_{SBIPA}$, respectively.

2.5. Electrochemical Evaluation

Electrochemical characterization was carried out in a conventional three-electrode setup of 125 mL. An ALS 2325 bipotentiostat (ALS Co., Ltd, Japan) combined with an RRDE-3A apparatus was used for fundamental experiments. Pt served as a counter electrode, and a saturated calomel electrode (SCE) as a reference electrode. All potential values within this paper were converted and are presented relative to RHE.

BOR measurements were carried out using cyclic and linear scan voltammetry. A 2 M NaOH solution was employed as the supporting electrolyte for all fundamental experiments. Cyclic voltammetry (CV) measurements were carried out in the potential range from OCP to 1.2 V applying scan rates from 5 to 1000 mV s^{-1}. Furthermore, the temperature effect was analyzed in the 25–65 °C temperature range. The BH_4^- concentration influence was studied in the 0.01–0.12 M range. Studies on the effect of temperature and concentration were conducted at a scan rate of 50 mV s^{-1}. RDE studies were carried out by linear scan voltammetry (LSV) at 10 mV s^{-1} by applying different rotation rates (0–2400 rpm). Apart from the concentration study, all experiments were conducted in a 0.03 M $NaBH_4$ in 2 M NaOH solution. Experiments were run at 25 °C and 0 rpm unless otherwise stated.

2.6. Fuel Cell Testing

A laboratory-scale direct borohydride peroxide fuel cell (DBPFC, V = 100 mL for both anodic and cathodic compartments) was assembled and tested. The two compartments were separated by a Nafion®117 (DuPont, Wilmington, DE, USA) cation-exchange membrane. A PAR 273A (Princeton Applied Research, Inc., Oak Ridge, TN, USA) potentiostat using PowerSuite software (PowerCV+ PowerSTEP) was employed for control of the experiments. The anolyte and catholyte were 1 M $NaBH_4$ in 4 M NaOH and 5 M H_2O_2 in 1.5 M HCl solutions, respectively. The chosen compositions are proven to be optimal in previous studies [99,100]. $PdAuNi/C_{SBIPA}$ was employed as the anodic catalyst (1 cm^2, 0.100 mg cm^{-2} catalyst loading, 0.012 mg cm^{-2} metal loading). The catalytic ink used for the anode was prepared as described in Section 2.4, with a GC tip used as substrate electrode. The cathode was a Pt mesh with a high surface area (Johnson Matthey, A = 50 cm^2) to ensure that fuel cell performance was not limited by the cathodic process. Interelectrode distance was the lowest possible to minimize ohmic resistance. DBPFC performance was analyzed in the 25–65 °C temperature range. Cell polarization curves were recorded, and the corresponding power density curves were plotted.

3. Results and Discussion

3.1. Physical Characterization Results

Figure 1 shows the XRD patterns of Pd/C and the three trimetallic catalysts. All catalysts showed one broad peak at 25°, typical of graphitic Vulcan carbon. For the monometallic Pd/C, the pattern showed four peaks that are characteristic of Pd (111), (200), (220), and (311) faces at 39.8°, 46.5°, 68.3°, and 82.1°, respectively (PDF#46-1043). However, for both trimetallic catalysts prepared by co-reduction (SBEG and SBIPA), there was a small shift in the peak positions to lower diffraction angles. This shift is ascribed to alloying among the three metals. Pd and Au, in particular, are well-known to exhibit remarkable alloying behavior [95,101–108]. Although Pd and Ni are known to form a solid solution for their bulk alloys, their potential for formulating a nanoalloy is lower [96,107–109]. It is not uncommon to see distinctive $Ni(OH)_2$ peaks at 60.1°, which is indicative of bulk Ni species segregation. In the present study, the shift in the two co-reduced trimetallic samples was suggestive of a nanoalloy formation among the metals. However, the appearance of $Ni(OH)_2$ peaks at 33.4° and 60.1° in the case of $PdAuNi/C_{SBEG}$ implied there was some Ni segregation in the bulk of that catalyst. Additionally, these $Ni(OH)_2$ peaks were also present in the three-step catalyst, although smaller than that of $PdAuNi/C_{SBEG}$.

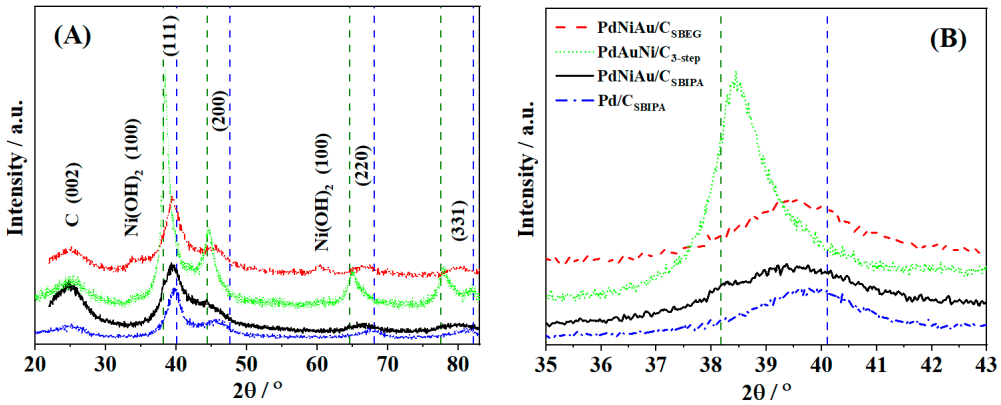

Figure 1. (**A**) XRD patterns of PdAuNi/C_{SBEG}, PdAuNi/C_{SBIPA}, Pd/C_{SBIPA}, and PdAuNi/$C_{3\text{-step}}$ and (**B**) the enlarged (111) facet for the four catalysts.

In contrast to PdAuN/$C_{3\text{-step}}$ and PdAuNi/C_{SBEG}, the catalyst synthesized via the SBIPA protocol did not show any individual Ni peaks. This indicated a higher potential of mixing of the three metals when the SBIPA protocol was used. KBr addition may also have contributed due to the replacement of the smaller Cl^- anion with Br^- during synthesis [110].

Unlike the SBEG and SBIPA catalysts, the XRD peaks of PdAuNi/$C_{3\text{-step}}$ were closer to pure Au (PDF#04-0784) than pure Pd (PDF#46-1043). This suggested the formation of Au@Pd (core@shell) structure as a consequence of the stepwise reduction process as previously reported [92,93]. Another important observation is that the XRD peak shift to lower diffraction angles was suggestive of the expansion of the Pd crystal lattice by the incorporation of the larger Au atoms into the Pd lattice. Ni is, theoretically, expected to contract the lattice, not to expand it. However, previous studies have found that adding Ni to Pd does not seem to displace the Pd diffraction peaks and therefore Ni does not necessarily contract the Pd lattice [59,111,112]. The peak shift in the case of PdAuNi/C_{SBEG} and PdAuNi/C_{SBIPA} is therefore consistent with lattice expansion and tensile strain that could upshift the *d*-band center and decrease the adsorbate-Pd bond strength [105].

The XRD Pd(111) peak of the four catalysts was analyzed to extract the peak broadening and diffraction angle values of each sample, and subsequently to determine their structural parameters: particle size, interplanar distance, and lattice constants (Table 1). The detailed analysis is explained in section "1. XRD calculation" of supplementary information (SI). While the interplanar distance and lattice constant were the same for Pd/C_{SBIPA}, PdAuNi/C_{SBIPA}, PdAuNi/C_{SBEG} (2.26 and 3.92 Å, respectively), it has increased in the case of PdAuNi/$C_{3\text{-step}}$ to 2.33 and 4.03 Å, respectively. It is noteworthy that the smallest particle size and highest broadening (FWHM) were those of PdAuNi/C_{SBIPA}, followed by the monometallic Pd/C_{SBIPA}, PdAuNi/C_{SBEG}, and, finally, PdAuNi/$C_{3\text{-step}}$. Factors other than crystallite size can also contribute to peak broadening, e.g., the instrument employed and the lattice strain. However, the Scherrer equation (Equation (S3)) is known to provide a reliable approximation of the crystallite size. The large particle size of PdAuNi/$C_{3\text{-step}}$ could be attributed to its Au-like structure, which presents larger lattice and interplanar distances.

Table 1. Structural and morphological parameters of Pd/C_{SBIPA}, PdAuNi/C_{SBIPA}, PdAuNi/C_{SBEG}, and PdAuNi/$C_{3\text{-step}}$.

Catalyst	$2\theta^\circ$	FWHM°	*d*-Space (Å)	*a* (Å)	τ_{XRD} (nm)
Pd/C_{SBIPA}	39.8	2.19	2.26	3.92	4.3
PdAuNi/C_{SBIPA}	39.4	2.47	2.26	3.92	3.8
PdAuNi/C_{SBEG}	39.6	2.32	2.26	3.92	4.9
PdAuNi/$C_{3\text{-step}}$	38.5	1.11	2.33	4.03	8.9

The bulk elemental composition of the synthesized catalysts was investigated by ICP-OES, as illustrated in Table 2. For Pd/C_{SBIPA}, the identified Pd loading was 12 wt.%, equivalent to the theoretical value. For $PdAuNi/C_{SBIPA}$, $PdAuNi/C_{SBEG}$, and $PdAuNi/C_{3\text{-step}}$, Pd loadings of 9 wt.%, 16 wt.%, and 22 wt.% were identified, respectively.

Table 2. ICP-OES metal composition of Pd/C_{SBIPA}, $PdAuNi/C_{SBIPA}$, $PdAuNi/C_{SBEG}$, and $PdAuNi/C_{3\text{-step}}$.

Catalyst	Pd/wt.%	Au/wt.%	Ni/wt.%
Pd/C_{SBIPA}	12	-	-
$PdAuNi/C_{SBIPA}$	5.1	2.6	0.7
$PdAuNi/C_{SBEG}$	4.8	0.8	9.9
$PdAuNi/C_{3\text{-step}}$	7.5	5.5	9.3

While ICP-OES determines the whole composition of the catalysts, the catalytically active sites are not dispersed throughout the bulk of the material. Instead, interaction with reactants takes place at surface sites. Therefore, the surface-weighted technique of EDX was used to gain insights into the composition of the catalysts in the catalytically relevant surface region. Figure 2 shows EDX metal elemental maps of $PdAuNi/C_{SBEG}$.

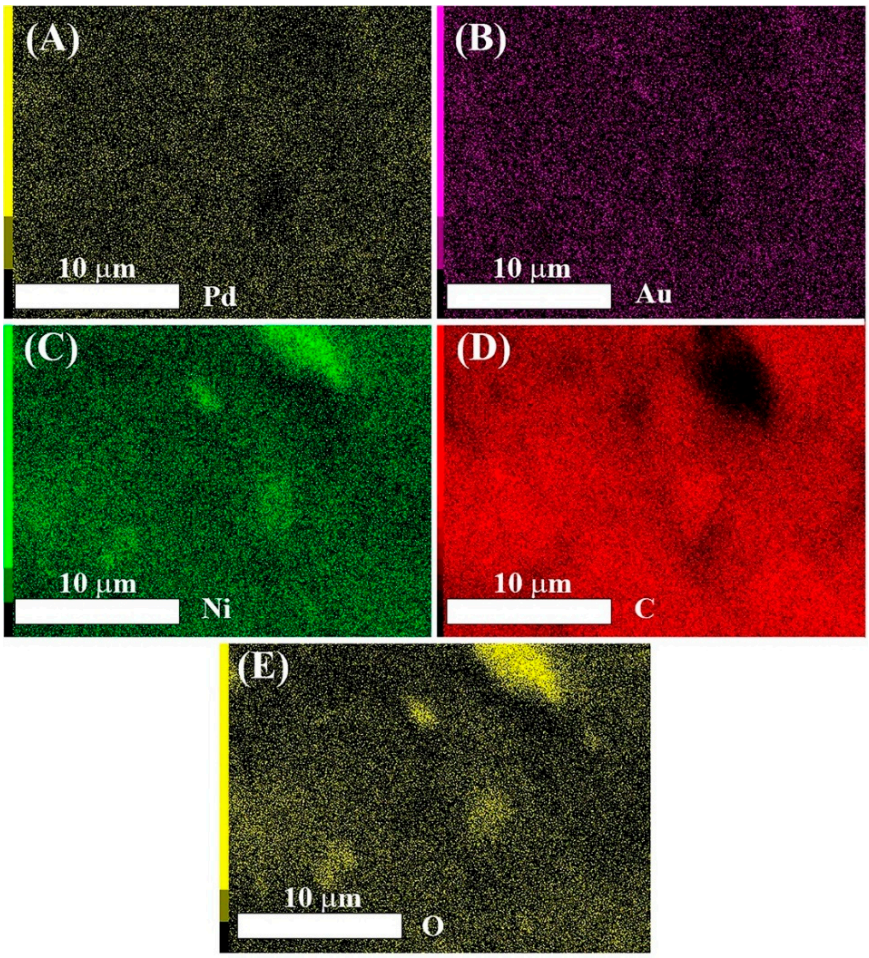

Figure 2. Elemental maps of (**A**) Pd, (**B**) Au, (**C**) Ni, (**D**) C, and (**E**) O obtained by EDX spectroscopy of $PdAuNi/C_{SBEG}$ at 10 kV.

While the Pd (A) and Au (B) maps show similar and relatively even distribution of both metals, the Ni map (C) shows three areas that were more densely populated with Ni species, indicating that Ni was not homogeneously distributed at the surface. The regions of high Ni density correspond to regions of low density in the C map (D) and in the O map

(E). This may suggest that some bulk segregation of $Ni(OH)_2$ had occurred, as supported by XRD data where a $Ni(OH)_2$ peak was observed, Figure 1.

Table 3 shows the quantitative composition data extracted from EDX in both weight and atomic percent for the three trimetallic catalysts investigated. This aimed to highlight the different surface metal segregation by applying two accelerating voltages: 10 kV and 20 kV, the latter providing greater surface penetration. Unlike Pd and Au, the atomic concentration of Ni at 10 kV was larger than that at 20 kV. This further confirms that Ni segregation to the catalyst surface occurred. EDX analyses revealed higher metal loading than either ICP-OES or the theoretical compositions, as the synthesis resulted in a heterogeneous composition throughout the carbon support, with metal preferentially located towards the surface, beneficial for catalysis.

Table 3. Quantitative EDX analysis of PdAuNi/C_{SBEG}, PdAuNi/$C_{3\text{-step}}$, and PdAuNi/C_{SBIPA} at 10 kV and 20 kV.

	PdAuNi/C_{SBEG}				**PdAuNi/$C_{3\text{-step}}$**				**PdAuNi/C_{SBIPA}**			
	10 kV		**20 kV**		**10 kV**		**20 kV**		**10 kV**		**20 kV**	
	wt.%	**at.%.**	**wt.%**	**at.%**	**wt.%**	**at.%.**	**wt.%**	**at.%**	**wt.%**	**at.%.**	**wt.%**	**at.%**
C	63.9	82.7	62.3	80.6	62.6	84.5	61.8	82.8	60.1	83.6	59.3	81.5
O	6.67	6.48	8.48	8.25	4.44	4.50	5.42	5.46	4.63	4.84	6.56	6.77
Ni	13.4	3.54	12.3	3.25	8.51	2.35	6.74	1.85	10.2	2.90	8.97	2.52
Pd	6.03	0.88	6.23	0.91	10.4	1.58	10.7	1.62	11.5	1.80	11.3	1.75
Au	3.82	0.30	3.93	0.31	7.96	0.66	8.17	0.67	7.92	0.67	7.56	0.63

Figure 3 shows the EDX maps of PdAuNi/C_{SBIPA}. Unlike PdAuNi/C_{SBEG}, the Au (A), Pd (B), and Ni (C) maps show that the three metals were co-located with high-density regions of one metal corresponding to high-density regions of the others. Areas of low metal density corresponded to density regions in the C map (D). This is anticipated, as at regions of low metal density, the bare C support was exposed at the surface. Although to a lesser extent than PdAuNi/C_{SBEG}, the quantitative data for PdAuNi/C_{SBIPA} (Table 3) indicated a slightly higher concentration of Ni at 10 kV (2.90 at.%) as compared to that at 20 kV (2.52 at.%), perhaps indicating some surface segregation of Ni for this material as well. Overall, PdAuNi/C_{SBIPA} showed relatively homogeneous metal distribution throughout the surface region, indicative of good mixing characteristics of the three metals in this case. This was further supported by the absence of any distinctive Ni peaks in this catalyst XRD pattern. Similar to PdAuNi/C_{SBIPA}, the EDX analysis of PdAuNi/$C_{3\text{-step}}$ revealed that Pd, Au, Ni, and C were co-located with each other (Figure S1), suggesting good mixing and little Ni segregation in this material.

Figure 4 shows representative TEM micrographs obtained for the Pd/C_{SBIPA}, PdAuNi/C_{SBIPA}, PdAuNi/C_{SBEG}, and PdAuNi/$C_{3\text{-step}}$ electrocatalysts, with additional TEM images being included in SI (Figures S2–S5). Examining the micrographs, the presence of highly dispersed metal nanoparticles on the carbon surface could be inferred. The very small particles indicated metal nanoparticles, while the large grey particles (40–60 nm) indicated the carbon aggregates. However, some particle aggregation and agglomeration could also be seen. This could be due to the synthesis method and/or being a monometallic system, which can promote particle growth and agglomeration more than a bimetallic or trimetallic one [56]. Comparing the trimetallic PdAuNi/C_{SBIPA} catalyst with the monometallic one prepared by applying the same protocol suggests that the latter explanation may apply in this case.

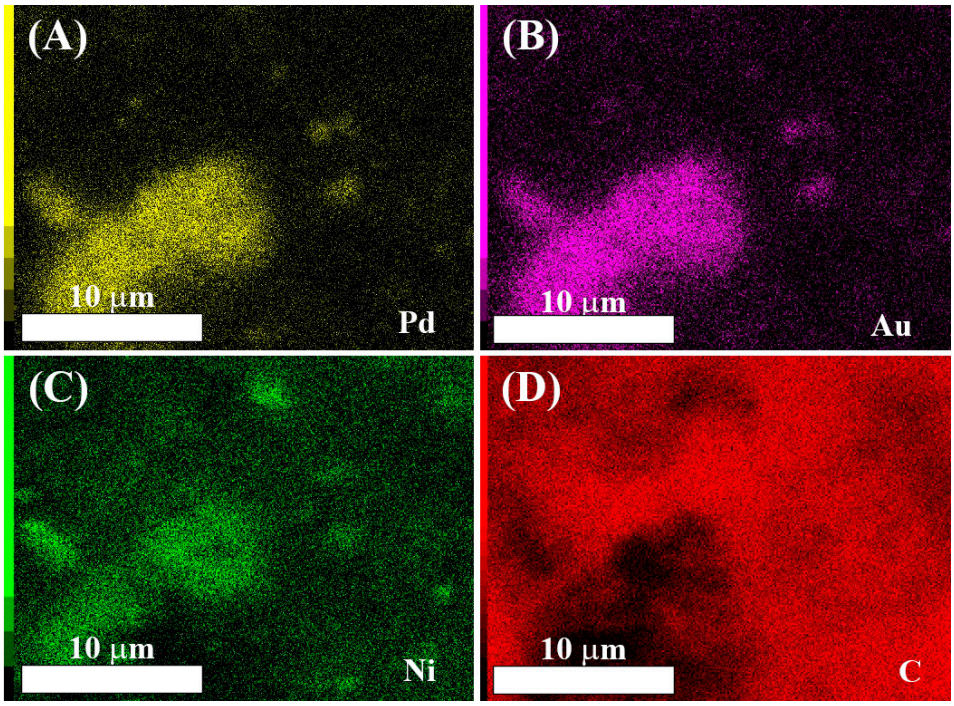

Figure 3. Elemental maps of (**A**) Pd, (**B**) Au, (**C**) Ni, and (**D**) C of PdAuNi/C_{SBIPA} obtained by EDX spectroscopy at 10 kV.

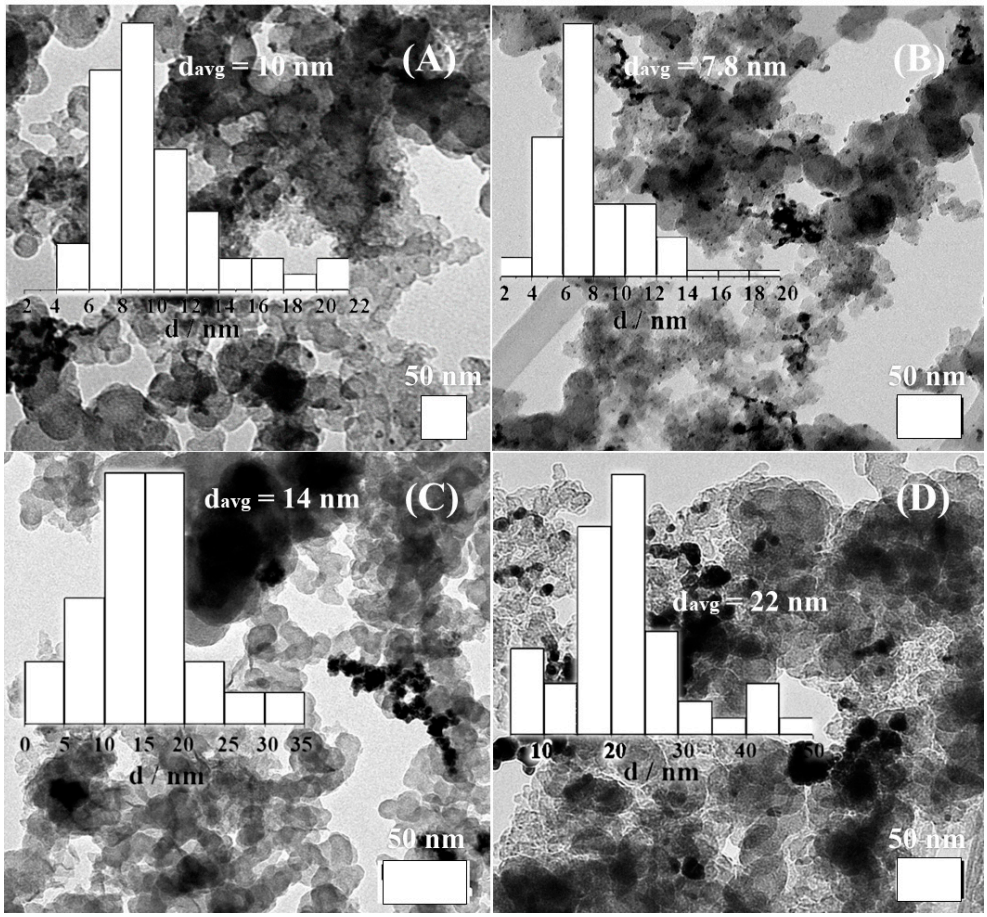

Figure 4. TEM micrographs and corresponding particle size distribution histograms of (**A**) Pd/C_{SBIPA}, (**B**) PdAuNi/C_{SBIPA}, (**C**) PdAuNi/C_{SBEG}, and (**D**) PdAuNi/$C_{3\text{-step}}$.

PdAuNi/C_{SBIPA} particles (1–6 nm, consistent with XRD analysis, Table 1) were very well dispersed, and less particle aggregation could be seen as compared to Pd/C. The reverse situation was noted for the PdAuNi/C_{SBEG}, which showed significant particle aggregation. Above those few carbon particles, high metal particle aggregation could be seen. This could be promoted by the $NaBH_4$-ethylene glycol reduction complex at 40 °C. Additionally, as discussed above with reference to the EDX map (Figure 3C), the high Ni content in this catalyst might contribute to this agglomeration, noting that Ni exists only in the form of $Ni(OH)_2$ (Figure 5).

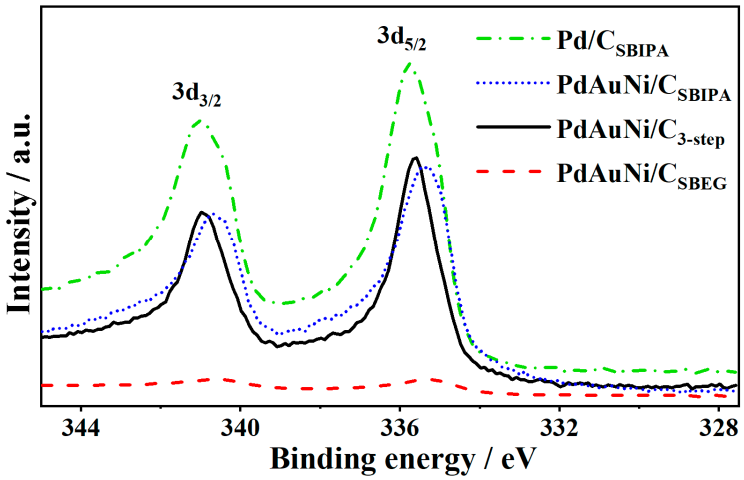

Figure 5. XPS spectra of Pd 3d in PdAuNi/C_{SBIPA}, Pd/C_{SBIPA}, PdAuNi/C_{SBEG}, and PdAuNi/$C_{3\text{-step}}$, showing Pd $3d_{3/2}$ and Pd $3d_{5/2}$ peaks.

The preparation method may also play a role in the promotion of agglomeration. For PdAuNi/C_{SBEG}, the metal precursors were initially mixed in ethylene glycol, followed by the slow addition of $NaBH_4$. Once the $NaBH_4$ addition commenced, the orange/brown solution turned black instantly, alongside the formation of bubbles. PdAuNi particles had most likely been reduced and segregated before the carbon support was added. For PdAuNi/$C_{3\text{-step}}$, on the other hand, Ni was initially reduced on the carbon surface (for 30 min), followed by Au (for 30 min), and finally Pd (for 30 min). As is clear from the XRD and EDX measurements, Ni segregation occurred once again, further verified by the observation of $Ni(OH)_2$ peaks, albeit in lower intensity than for PdAuNi/C_{SBEG}. Additionally, Au had most likely formed a core@shell structure with Pd, since the XRD pattern was more representative of Au than of Pd. Although to a lesser degree than PdAuNi/C_{SBEG}, significant particle aggregation was observed, and particle size was the largest in comparison to the other catalysts. Following PdAuNi/$C_{3\text{-step}}$, PdAuNi/C_{SBEG} particle size was larger than that of both Pd/C_{SBIPA} and PdAuNi/C_{SBIPA}. The PdAuNi particle sizes obtained were slightly smaller than previously reported for trimetallic systems [68,69].

Figure 5 shows the XPS measured data for the Pd 3d peak positions of the four catalysts. The molar Pd:Au:Ni ratio of PdAuNi/C_{SBIPA} equaled 64:17:19, while it was 5:1:94 and 58:6:36 for PdAuNi/C_{SBEG} and PdAuNi/$C_{3\text{-step}}$, respectively. This showed the abundant Pd presence on the surface of PdAuNi/$C_{3\text{-step}}$ and PdAuNi/C_{SBIPA} samples, while PdAuNi/C_{SBEG} contained mainly Ni (94 at.%) and only 6 at.% Pd and Au combined. Furthermore, it is noteworthy that the highest oxygen content (5.19 at.%) existed in PdAuNi/C_{SBEG}, likely a consequence of the presence of significant $Ni(OH)_2$ (2.19 at.%). The Pd 3d peak of Pd/C_{SBIPA} (Table S1 in SI) could be deconvoluted into a high-energy band corresponding to Pd $3d_{3/2}$ (340.73 eV) and a low-energy band corresponding to Pd $3d_{5/2}$ (335.43 eV). Those bands were shifted approximately 0.40 eV to higher binding energy compared to pure Pd, due to the interaction with the C support. Moreover, the Pd 3d binding energies of PdAuNi/C_{SBEG} and PdAuNi/C_{SBIPA} samples were shifted ~0.5 eV and 0.15 eV, respectively, to lower binding energies. On the contrary, Pd 3d of PdAuNi/$C_{3\text{-step}}$

was shifted 0.05 eV to binding energy higher than that of the Pd/C_{SBIPA} sample. Pd 3d peak positions are shown in Figure 5. Ni 2p and Au 4f were also shifted in the three trimetallic samples compared to pure Au and Ni, the binding energies of which were 84 eV and 855.6 eV ($Ni(OH)_2$), respectively. While the Ni peaks shifted towards higher binding energy compared to pure Ni, the reverse trend was observed for Au. The Ni 2p shift was estimated to be +0.3 eV, +0.7 eV, and +0.8 eV for PdAuNi/C_{SBIPA}, PdAuNi/C_{SBEG}, and PdAuNi/$C_{3\text{-step}}$, respectively. The Au 4f shift was −0.3 eV, −0.4 eV, and −0.2 eV for PdAuNi/C_{SBIPA}, PdAuNi/C_{SBEG}, and PdAuNi/$C_{3\text{-step}}$, respectively. The shift in the binding energy was indicative of a change in the adsorption behavior of the respective catalysts. The presence of Au and Ni potentially explains why PdO was not detected in the trimetallic sample, unlike in the monometallic one, which contained 20 wt.% of Pd as PdO. Adding both Au and Ni enhanced Pd air stability. The full XPS surveys are illustrated in Figure S6. The individual elemental (Pd 3d, Au 4f, and Ni 2p) XPS peaks are available in Table S1, which confirms that Pd and Au existed in the metallic state in the trimetallic samples, Pd existed in metallic and oxide form in the monometallic sample, and Ni predominantly existed as $Ni(OH)_2$. The Ni 2p peak in the PdAuNi/C_{SBIPA} sample contained some Ni metal alongside $Ni(OH)_2$, unlike PdAuNi/C_{SBEG} and PdAuNi/$C_{3\text{-step}}$. This further exemplifies the good mixing of the three metals obtained by the SBIPA protocol, which was corroborated by the XRD and EDX data.

PdAuNi/C_{SBEG} has furthermore achieved the highest shift of Pd 3d to the left, which was also the broadest from the four-sample Pd 3d peaks as reported for the addition of Ni to Pd [108]. Examining the Ni 2p peaks of the three trimetallic samples, two high-binding-energy satellite peaks were adjoined to the main peaks of Ni, which indicates Ni multi-electron excitations [59,96,111,112]. Additionally, in the case of PdAuNi/C_{SBEG} and PdAuNi/$C_{3\text{-step}}$ samples, the single pattern of two Ni 2p peaks suggests the presence of only one oxide species, $Ni(OH)_2$, in contrast to the findings of Ramulifho et al. [113]. In terms of co-reduction, Au is the easiest of the three metals to reduce, followed by Pd. On the contrary, Ni is the slowest to reduce [95,114]. Therefore, it may not be incorrect to assume that the surface of the trimetallic catalysts (especially PdAuNi/C_{SBEG}) was richest in Ni and poor in Au, which was evident from the XPS and EDX measurements. On the other hand, the core would be highly populated with Au and lacking a substantial Ni proportion.

3.2. Borohydride Oxidation Reaction Studies

The catalytic performance of the three PdAuNi/C electrocatalysts towards the BOR was initially investigated by scanning comparative CVs in 2 M NaOH with 0.03 M $NaBH_4$ and in pure 2 M NaOH. Along with evaluating the activity of the synthesized trimetallic catalysts, the response of monometallic Pd/C was also evaluated in order to better understand the role played by Au and Ni. The CVs of three catalysts as well as of monometallic Pd/C depicted in Figure 6A–C show the absence of any relevant anodic peaks in the BOR potential region in NaOH solution, implying that the current generated during CVs recorded in the presence of BH_4^- originated from its oxidation. Based on the shape of the CVs and similar OCP values of ca. −0.12 V, it could be assumed that the studied catalysts promoted similar reaction mechanisms. Similar OCP values were reported in other recent studies on BOR at Pd-containing materials [53,54]. Within the scanned potential range, CVs of three different catalysts showed two oxidation peaks in the positive scan, while an additional sharp oxidation peak was evident in the reverse scan. The first oxidation peak appeared as a wide oxidation hump at ca. 0.29 V for the PdAuNi/C_{SBEG} and PdAuNi/C_{SBIPA} catalysts, while in the case of PdAuNi/$C_{3\text{-step}}$, this peak was more pronounced and positioned at more positive potential (0.38 V). It is believed that this peak can be attributed to H_2 oxidation, which originates from the borohydride hydrolysis reaction, and to the initial oxidation of adsorbed BH_3OH^- [54]. The second anodic peak at ~0.8 V for all examined samples can be considered to originate from electrooxidation of BH_4^- as well as BH_3OH^- [48,54]. PdAuNi/C_{SBIPA} gave the best catalytic response,

reaching the peak current density of 46 mA cm^{-2} at 50 mV s^{-1}, a value considerably higher than those reached employing carbon-supported Pd-Cu [115], Pd-Au [116], and Au-Ni [117] alloy nanoparticles. Additionally, the oxidation peak on the cathodic scan in the potential window from 0.5 to 0.8 V for all three studied samples was most likely related to the oxidation of BH_3OH^- [118], which was formed during the anodic scan and stayed adsorbed on the oxidized electrode surface until it was reactivated by reduction of the surface oxides.

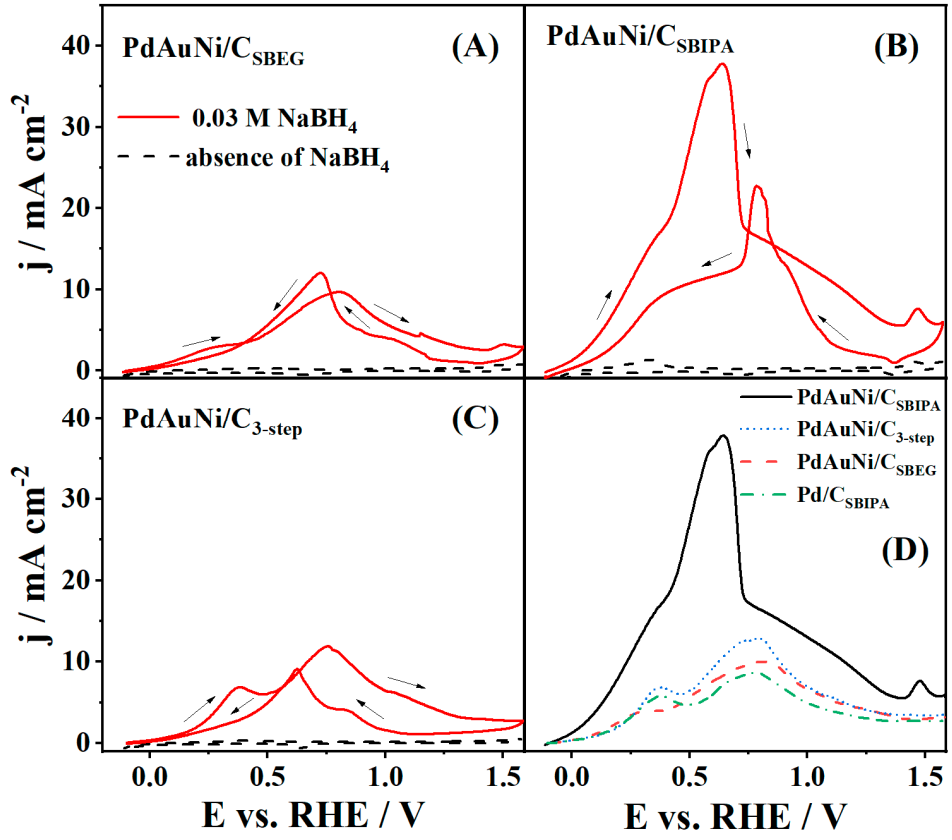

Figure 6. CVs (third cycle) in the absence (2 M NaOH) and presence (2 M NaOH + 0.03 M $NaBH_4$) of BH_4^- for (**A**) PdAuNi/C_{SBEG}, (**B**) PdAuNi/C_{SBIPA}, and (**C**) PdAuNi/$C_{3\text{-step}}$ electrocatalysts, and (**D**) comparative CVs of trimetallic and Pd/C_{SBIPA} monometallic catalysts in the presence of BH_4^-. CVs ran at 50 mV s^{-1} and 25 °C.

The catalytic performance of the synthesized materials was further compared with the response obtained for monometallic Pd/C_{SBIPA}. Figure 6D reveals the inferior catalytic activity of Pd/C_{SBIPA}. Introducing Au and Ni into Pd provided more active sites where BH_4^- adsorption could take place and as such, trimetallic catalysts were expected to exhibit higher activity towards BOR. Improved catalytic properties can be explained by the produced synergistic effect of combining Pd with Au, a metal that is relatively inert towards hydrolysis, and Ni, a 3d transition metal, and the resultant electronic effect. In terms of electronic interaction, as XPS results suggest, the addition of Ni may have influenced the atomic band structure of the other two metals. This can further lead to the reduced adsorption energy of BOR intermediates, thus preserving those active sites for BH_4^- adsorption and further encouraging BOR activity [119].

The PdAuNi/C_{SBIPA} highest catalytic activity most likely resulted from the absence of segregation of Ni. This enabled an improved degree of alloying in comparison with the other two studied catalysts, as confirmed by XRD results. Additionally, the enhanced catalytic activity of PdAuNi/C_{SBIPA} could also be associated with the better dispersed multi-metallic particles of smaller average size, confirmed by TEM analysis and the re-

spective EDX elemental maps. Smaller particle size and interparticle distance produced larger surface area and, therefore, were deemed beneficial for catalytic reactions. However, caution must be practiced as Antolini et al. [120] reviewed that decreasing the particle size below 5 nm and interparticle distance below 20 nm adversely impacts the reduction of oxygen, as well as reactions of ethanol and methanol oxidation on Pt surfaces. The situation would be worse for a highly aggregated particle system due to exceedingly smaller interparticle distance. That is a likely reason for the lower PdAuNi/C_{SBEG} performance in the present study. The CVs shown in Figure 6 are also available in specific current density (mA $mg_{metal}{}^{-1}$) in SI (Figure S7).

BOR kinetic parameters are summarized in Table 4 for each catalyst.

Table 4. Kinetic parameters for BOR at the four studied catalysts.

Catalyst	α	n	β	E_a/kJ mol^{-1}
PdAuNi/C_{SBEG}	0.60	2.8	0.91	34.0
PdAuNi/C_{SBIPA}	0.75	7.1	1.00	16.7
PdAuNi/$C_{3\text{-step}}$	0.73	7.4	1.12	29.9
Pd/C_{SBIPA}	0.70	1.2	0.94	28.9

For all samples, an upward trend of current density with increasing polarization rate, as well as a small shift in the position of the characteristic $BH_4{}^-$ oxidation peak to more positive potentials were observed. Figure 7A illustrates this behavior for PdAuNi/C_{SBIPA} as the best material. This allowed for the determination of the charge transfer coefficient (α) values using the expression describing the peak potential dependence on the logarithm of polarization rate (E_p vs. ln ν) for irreversible processes [12,121]. The values were found to be relatively similar for all studied catalysts (Table 4), with PdAuNi/C_{SBIPA} showing the highest α value. High values indicate that BOR at examined electrocatalysts was an irreversible and diffusion-controlled process. The obtained values are comparable to the ones reported for catalysts containing Pd, Au, and Ni [12,25,47,79,100,121].

In the case of PdAuNi/C_{SBIPA} (Figure 7B), a significant increase in anodic current densities when recording the CVs starting from 0.01 M to 0.12 M $NaBH_4$ concentration was evident. The CVs revealed that the anodic current density value amounted to 8.5 mA cm^{-2} for the lowest concentration (0.01 M), while a value nine times higher was achieved for the highest $NaBH_4$ concentration. The observed trend corresponded to enhanced mass transfer, and this behavior agrees with previous reports employing Au-, Pd-, and/or Ni-based electrocatalysts [48,78,79,122,123]. In addition, the oxidation process started at lower potentials but reached its maximum at more positive potential values. The order of reaction (β) values was obtained using ln j vs. ln c plot slope and ranged from 0.91 for PdAuNi/C_{SBEG} to 1.12 for PdAuNi/$C_{3\text{-step}}$.

CVs obtained at elevated temperatures also exhibited higher current densities for all studied electrocatalysts. This behavior was expected, since higher temperatures lead simultaneously to a decrease in solution viscosity, resulting in a higher $BH_4{}^-$ diffusion coefficient, and faster electron transfer kinetics. By constructing the Arrhenius plots [121], depicted in the inset of Figure 7C, and applying the Arrhenius equation, the values of the apparent activation energy, $E_a{}^{app}$, were estimated. PdAuNi/C_{SBIPA} showed the lowest value of 16.7 kJ mol^{-1}, while the highest value of this parameter was observed for PdAuNi/C_{SBEG} (34 kJ mol^{-1}). Similar values were reported for mono- and bimetallic noble metal or/and transition metal-containing materials. For instance, BOR at carbon-supported Pd catalyst (prepared using different synthesis methods and types of carbon support) [53,124] has been shown to proceed with activation energy ranging from as low as 10 kJ mol^{-1} to 26 kJ mol^{-1}. Moreover, $E_a{}^{app}$ of BOR at a commercially available Pt/C [22] catalyst was reported to have a value of 34 kJ mol^{-1}, while alloying with transition metals (Co and Ni) resulted in lower values (25 and 20 kJ mol^{-1}, respectively).

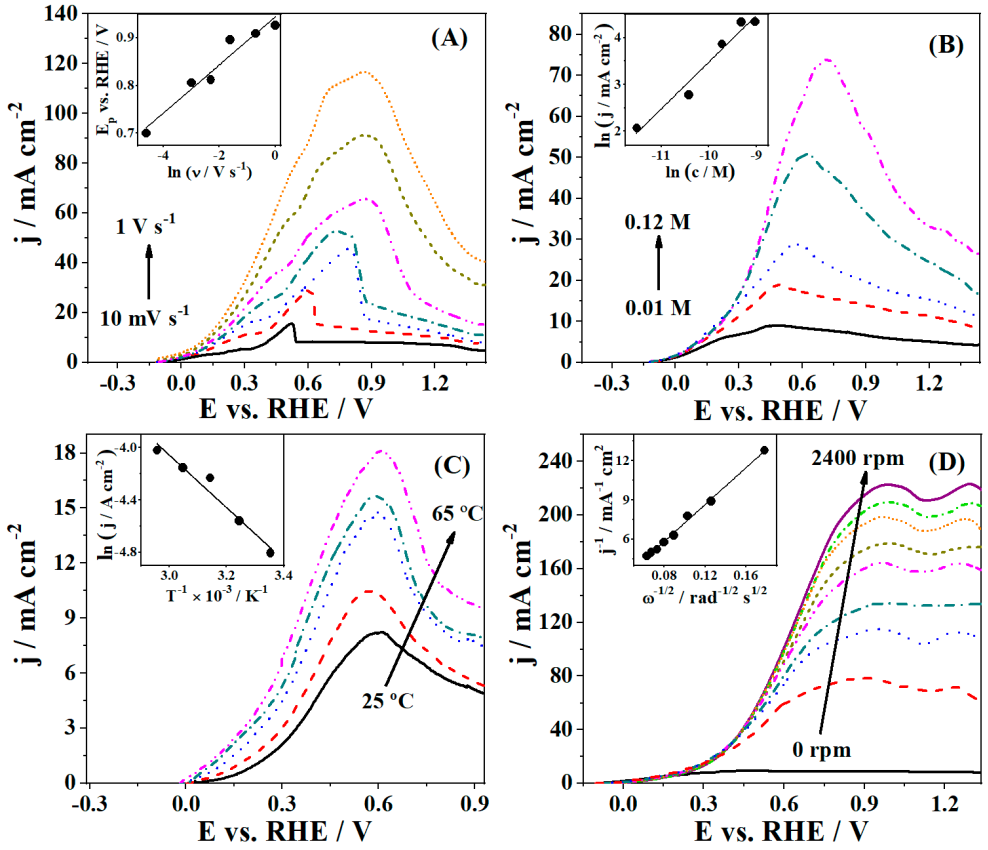

Figure 7. CVs of PdAuNi/C_{SBIPA} at (**A**) different scan rates, ν, and the derived E_p vs. ln ν plots (inset), (**B**) different $NaBH_4$ concentrations and the derived ln j vs. ln c plots (inset), (**C**) different temperatures and the derived Arrhenius plots (inset), and (**D**) LSVs of PdAuNi/C_{SBIPA} at 10 mV s^{-1} and different rotation rates and the derived Koutecky–Levich plot (inset). The electrolyte solution used was 0.03 M $NaBH_4$ + 2 M NaOH, polarization rate was 50 mV s^{-1}, with room temperature (25 °C), unless otherwise noted.

The reaction kinetics were additionally examined using RDE LSVs, and polarization curves were obtained; the corresponding j^{-1} vs. $\omega^{-1/2}$ plot for the currents taken at 0.9 V (inset) is shown in Figure 7D. From the slope of j^{-1} vs. $\omega^{-1/2}$ plots and using the Koutecky–Levich equation, n values were obtained [125]. The shift of half-wave potential with an increase of the electrode rotation speed confirmed the irreversibility of the reaction.

The n values for PdAuNi/$C_{3\text{-step}}$ and PdAuNi/C_{SBIPA} electrocatalysts (7.4 and 7.1, respectively) were determined to nearly match the theoretical value of 8, while significantly lower values were obtained for the other two materials (2.8 and 1.2 for PdAuNi/C_{SBEG} and Pd/C_{SBIPA}, respectively). Although in terms of current densities, PdAuNi/$C_{3\text{-step}}$ showed significantly lower values than PdAuNi/C_{SBIPA}, the highest n value could be explained by Au@Pd (core@shell) structure formation previously identified in the XRD analysis. Such a structure makes the behavior of the catalyst more Au-like due to the core position of those nanoparticles and as such, less active toward the BH_4^- hydrolysis reaction [12,100,126]. The lower faradaic efficiency of PdAuNi/C_{SBEG} and Pd/C_{SBIPA} was most likely a consequence of the higher hydrolysis rates at those two electrocatalysts. Obtained n values for PdAuNi/C_{SBEG} and Pd/C_{SBIPA} are similar to the ones obtained for other Pd-containing materials reported in previous studies. For instance, Martins et al. [54] reported n values of 2 and 5.6 during BOR at Pd nanoparticles with two different types of biobased carbon supports. For other Pd-based catalysts, depending on $NaBH_4$ concentration, n values between 2 and 6 [53,118] were obtained, indicating hydrolysis occurrence in parallel with the oxidation of BH_4^-. Song et al. [127] recently reported high BOR current densities for a ternary CuPdNi electrode, but at high overpotentials and an n value of 4.9, far from those obtained for the two best catalysts in this work. Alloying Pd

with Au resulted in n ~6, as reported by Simões et al. [57], also lower than values than obtained herein for PdAuNi/C_{SBEG} and Pd/C_{SBIPA}. Figure 7 is also available in specific current density (Figure S8 of SI).

3.3. Fuel Cell Testing

Figure 8 (available in SI in specific current density, Figure S9) depicts the polarization and power density curves of a single cell with PdAuNi/C_{SBIPA} anode operating at two different temperatures, 25 and 75 °C, along with anode and cathode potentials measured during the cell operation and experimentally measured cell voltage. The cathode potential measured in zero current regime (open-circuit conditions) at 25 °C was almost identical to the equilibrium potential of H_2O_2 reduction given in Equation (4) (E^0 = 1.78 V), suggesting direct H_2O_2 reduction. As for the cell operating at elevated temperature (75 °C), this value was slightly less positive, as expected, implying H_2O_2 disproportionation was followed by O_2 reduction to a certain extent [18,21]. On the other hand, the anode potential measured during the experiment was significantly higher than the equilibrium potential for BOR described by Equation (1), implying that the anodic process also involved side reactions, such as oxidation of H and BH_3OH^- generated during spontaneous hydrolysis of BH_4^- [128]. Moreover, from Figure 8B,C, a small difference between cell voltage, E_{cell}, and the calculated potential difference of the half-reactions, E_c–E_a, could be observed, which revealed minor resistance of system components.

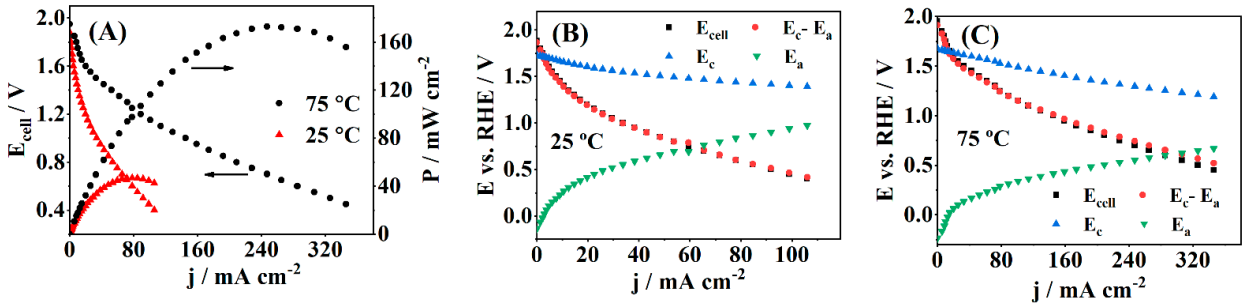

Figure 8. (**A**) Polarization and power density curves at 25 and 75 °C for a DBPFC using a PdAuNi/C_{SBIPA} anode and a Pt cathode. The cathode and anode potentials, their potential difference, and E_{cell} are also represented at (**B**) 25 °C and (**C**) 75 °C.

Considering the pH values of electrolytes, the theoretical voltage value of such fuel cells was expected to be close to 3 V. However, the cell polarization curves show an OCV value of ~1.9 V at both temperatures. This fluctuation in OCV value was mainly triggered by the mixed potential occurrence on the anodic side and it agrees with the reports from the literature for DBPFCs studies performed under conditions similar to the ones reported herein [18,125,128]. After the initial voltage decay due to activation losses, cell voltage continued to decrease linearly with current density, while mass transport effects were not evident. The power density value reached its maximum of 47.5 mW cm^{-2} at 0.6 V and 78 mA cm^{-2}. As expected, at an elevated temperature of 75 °C, the kinetics of both fuel cell reactions (BOR and HPRR) was faster, and a significant improvement in cell performance was displayed. The maximum value of power density that was obtained at this temperature was almost four times higher than that at 25 °C, amounting to 175 mW cm^{-2}. This value was exhibited at a cell voltage value of 0.7 V, while current density reached 247 mA cm^{-2}. The comparison of the DBPFC results obtained herein with the ones from the literature is shown in Table 5.

Table 5. Comparison of the DBPFC parameters obtained in this work with those reported in similar studies using Pd, Au, Ni, and their alloys.

Anode	Cathode	Fuel	Oxidant	T/°C	OCV/V	P/mW cm^{-2}	$E_{cell,\ peak}$/V	Ref.
PdAuNi/C_{SBIPA}	Pt	1 M $NaBH_4$ + 4 M NaOH	5 M H_2O_2 + 1.5 M HCl	25 75	1.90 1.90	47.5 175	0.60 0.70	This work
Au/C	Pt	0.5 M $NaBH_4$ + 2 M NaOH	4.5 M H_2O_2 + 2 M HCl	20	1.41	8.72	0.42	[119]
AuCu/C	Pt	0.5 M $NaBH_4$ + 2 M NaOH	4.5 M H_2O_2 + 2 M HCl	20	1.50	31.3	0.49	[119]
AuNi/C	Pt	0.5 M $NaBH_4$ + 2 M NaOH	4.5 M H_2O_2 + 2 M HCl	20	1.59	40.6	0.57	[119]
$Au_{1.5}$NiCu/C	Pt	0.5 M $NaBH_4$ + 2 M NaOH	4.5 M H_2O_2 + 2 M HCl	20	1.62	47.4	0.70	[119]
Au_2NiCu/C	Pt	0.5 M $NaBH_4$ + 2 M NaOH	4.5 M H_2O_2 + 2 M HCl	20	1.78	60.5	0.88	[119]
Au/C	Au/C	1 M $NaBH_4$ + 3 M NaOH	2 M H_2O_2 + 0.5 M H_2SO_4	25	1.87	28.2	0.59	[129]
$Au_{45}Co_{55}$/C	Au/C	1 M $NaBH_4$ + 3 M NaOH	2 M H_2O_2 + 0.5 M H_2SO_4	25	1.92	66.5	0.77	[129]
Ni@Pd/PANI [1]	Pt/C	1 M $NaBH_4$ + 2 M NaOH	2 M H_2O_2 + 1.5 M HCl	60	1.76	120	0.61	[130]
PtNi/C	Pt/C	1 M $NaBH_4$ + 2 M NaOH	2 M H_2O_2 + 0.5 M H_2SO_4	60	1.77	107	0.82	[131]
Pd/MWCNT	Pt/MWCNTs [2]	5 wt.% $NaBH_4$ + 10 wt.% NaOH	5 wt.% H_2O_2 + 5 wt.% H_2PO_4	25	1.80	119	0.58	[128]

[1] Ni@Pd (core@shell structure) supported on polyaniline (PANI). [2] Pt supported on multiwalled carbon nanotubes (MWCNTs).

PdAuNi/C_{SBIPA} exhibited the best performance among the presented electrocatalysts, even when compared with the typical (and expensive) electrocatalysts exclusively composed of noble metals (e.g., Pd [128], Au/C [129]). It shows that the alloying effect, especially between noble and low-cost metals, is one of the best ways to decrease the price of electrocatalysts while increasing their catalytic activity. In fact, the highest activity of PdAuNi/C_{SBIPA} towards BOR, i.e., the most pronounced synergistic effect, might be due to the complete mixing of three metals by the SBIPA procedure, as indicated by XRD analysis. Furthermore, XRD and XPS analysis indicated the decrease of adsorbate-Pd bond strength that could lead to faster release and subsequent oxidation of the reaction intermediates. Thus, PdAuNi/C_{SBIPA} was demonstrated to be 1.5 and 1.6 times more active (in terms of current density) for BOR than Ni@Pd/PANI [130] and PtNi/C [131] electrocatalysts, which reflects the advantage of using a trimetallic alloy, probably due to the mentioned synergic effect. Carbon-supported $Au_xNi_yCu_z$ trimetallic electrocatalysts [119] exhibited better results than PdAuNi/C_{SBIPA} at high Au amounts (Au_2NiCu). For the other compositions, PdAuNi/C_{SBIPA} was demonstrated to be a more effective anode, showing that the affinity between the metals is crucial to promote a notable alloying effect.

4. Conclusions

PdAuNi carbon-supported trimetallic catalysts were successfully synthesized by three different routes. A PdAuNi/C_{SBIPA} catalyst, synthesized via reduction using a $NaBH_4$-2-propanol complex, presented the best alloying effect, while the other two materials showed the presence of segregated Ni species, as confirmed by XRD, TEM, and XPS analyses. The results obtained from CV and LSV measurements revealed that the catalysts performed well towards BOR. The PdAuNi/C_{SBIPA} catalyst exhibited the highest activity, evidenced by the high number of exchanged electrons amounting to 7.1, and the lowest apparent activation energy (ca. 16.7 kJ mol^{-1}). Furthermore, DBPFC operating at two different temperatures (25 and 75 °C) employing a PdAuNi/C_{SBIPA} anode showed a maximum power density of 47.5 mW cm^{-2} at 25 °C, with a significant improvement with a temperature increase and peak power density of 175 mW cm^{-2} at 75 °C. Considering the economic benefits of alloying and using support materials, and the results obtained herein, it can be concluded that PdAuNi/C_{SBIPA} is an interesting candidate for the application in DBPFC as anode material.

Supplementary Materials: The following are available online at https://www.mdpi.com/article/10.3390/nano11061441/s1, Figure S1: (A) Pd, (B) Au, and (C) Ni elemental maps of PdAuNi/$C_{3\text{-step}}$ obtained by EDX spectroscopy at 20 kV, Figure S2: TEM images of Pd/C_{SBIPA} electrocatalyst, Figure S3: TEM image of PdAuNi/C_{SBIPA} electrocatalyst, Figure S4: TEM image of PdAuNi/C_{SBEG} electrocatalyst, Figure S5: TEM images of PdAuNi/$C_{3\text{-step}}$ electrocatalyst, Figure S6: XPS survey spectra of Pd/C_{SBIPA}, PdAuNi/C_{SBIPA}, PdAuNi/C_{SBEG}, and PdAuNi/$C_{3\text{-step}}$, Figure S7: CVs (third cycle) in 2 M NaOH + 0.03 M $NaBH_4$ for (A) PdAuNi/C_{SBEG}, (B) PdAuNi/C_{SBIPA}, and (C) PdAuNi/$C_{3\text{-step}}$ electrocatalysts and (D) comparative CVs of trimetallic and Pd/C_{SBIPA} monometallic catalysts. CVs run at 50 mV s^{-1} and 25 °C, Figure S8: CVs of PdAuNi/C_{SBIPA} at (A) different scan rates, ν, and the derived E_p vs. ln ν plots (inset), (B) different $NaBH_4$ concentrations and the derived ln j vs. ln c plots (inset), (C) different temperatures and the derived Arrhenius plots (inset), and (D) LSVs of PdAuNi/C_{SBIPA} at 10 mV s^{-1} and different rotation rates and the derived Koutecky–Levich plot (inset). The electrolyte solution used was 0.03 M $NaBH_4$ + 2 M NaOH, polarization rate was 50 mV s^{-1}, and room temperature (25 °C), unless otherwise noted, Figure S9: (A) Polarization and power density curves at 25 and 75 °C for a DBPFC using a PdAuNi/C_{SBIPA} anode and a Pt cathode. The cathode and anode potentials, their potential difference, and E_{cell} are also represented at (B) 25 °C and (C) 75 °C., Table S1: XPS elemental peaks of Pd 3d, Au 4f, and Ni 2p in Pd/C_{SBIPA}, PdAuNi/C_{SBIPA}, PdAuNi/C_{SBEG}, and PdAuNi/$C_{3\text{-step}}$.

Author Contributions: Conceptualization, C.A.C.S., B.Š., J.M., and D.M.F.S.; formal analysis, A.M.A.E., G.B., and R.C.P.O.; investigation, A.M.A.E. and G.B.; writing—original draft preparation, A.M.A.E., G.B., R.C.P.O., and C.A.C.S.; writing—review and editing, J.M., B.Š., and D.M.F.S., visualization, A.M.A.E., R.C.P.O. and D.M.F.S.; supervision, J.M., B.Š., and D.M.F.S. All authors have read and agreed to the published version of the manuscript.

Funding: This research was funded by a Newton-Mosharafa Scholarship NMJ8/15 (A. Elsheikh) and by the Portuguese Foundation for Science and Technology (FCT, Portugal) through a research grant within project UID/CTM/04540/2013 (G. Backović), a research contract in the scope of programmatic funding UIDP/04540/2020 (D.M.F. Santos), a Ph.D. grant SFRH/BD/137470/2018 (R.C.P. Oliveira), and contract no. IST-ID/156/2018 (B. Šljukić).

Data Availability Statement: The data presented in this study are available on request from the corresponding author.

Conflicts of Interest: The authors declare no conflict of interests. The funders had no role in the design of the study; in the collection, analyses, or interpretation of data; in the writing of the manuscript, or in the decision to publish the results.

References

1. Larminie, J.; Dicks, A. *Fuel Cell Systems Explained*, 3rd ed.; John Wiley & Sons Ltd.: London, UK, 2018. [CrossRef]
2. Kreuer, K.D. Fuel Cells, Introduction. In *Fuel Cells*; Kreuer, K.D., Ed.; Springer: New York, NY, USA, 2013. [CrossRef]
3. Maiyalagan, T.; Saji, V.S. *Electrocatalysts for Low Temperature Fuel Cells*; Wiley-VCH Verlag GmbH & Co. KGaA: Weinheim, Germany, 2017. [CrossRef]
4. Akay, R.G.; Yurtcan, A.B. *Direct Liquid Fuel Cells: Fundamentals, Advances and Future*, 1st ed.; Academic Press: Cambridge, MA, USA, 2020. [CrossRef]
5. Demirci, U.B. Direct borohydride fuel cell: Main issues met by the membrane–electrodes-assembly and potential solutions. *J. Power Sources* **2007**, *172*, 676–687. [CrossRef]
6. Indig, M.E.; Snyder, R.N. Sodium Borohydride, An Interesting Anodic Fuel (1). *J. Electrochem. Soc.* **1962**, *109*, 1104–1106. [CrossRef]
7. Vielstich, W.; Lamm, A.; Gasteiger, H. *Handbook of Fuel Cells: Fundamentals, Technology, Applications, 4 Volume Set*; John Wiley & Sons, Inc.: Hoboken, NJ, USA, 2003.
8. Ma, J.; Choudhury, N.A.; Sahai, Y. A comprehensive review of direct borohydride fuel cells. *Renew. Sustain. Energy Rev.* **2010**, *14*, 183–199. [CrossRef]
9. de Leon, C.P.; Walsh, F.; Pletcher, D.; Browning, D.; Lakeman, J. Direct borohydride fuel cells. *J. Power Sources* **2006**, *155*, 172–181. [CrossRef]
10. Ong, B.; Kamarudin, S.; Basri, S. Direct liquid fuel cells: A review. *Int. J. Hydrogen Energy* **2017**, *42*, 10142–10157. [CrossRef]
11. Rostamikia, G.; Janik, M.J. Direct borohydride oxidation: Mechanism determination and design of alloy catalysts guided by density functional theory. *Energy Environ. Sci.* **2010**, *3*, 1262–1274. [CrossRef]
12. Santos, D.M.F.; Sequeira, C.A.C. Cyclic voltammetry investigation of borohydride oxidation at a gold electrode. *Electrochim. Acta* **2010**, *55*, 6775–6781. [CrossRef]
13. Lima, F.H.; Pasqualeti, A.M.; Concha, M.B.M.; Chatenet, M.; Ticianelli, E.A. Borohydride electrooxidation on Au and Pt electrodes. *Electrochim. Acta* **2012**, *84*, 202–212. [CrossRef]
14. Arevalo, R.L.; Escaño, M.C.S.; Wang, A.Y.-S.; Kasai, H. Structure and stability of borohydride on Au(111) and Au3M(111) (M = Cr, Mn, Fe, Co, Ni) surfaces. *Dalton Trans.* **2013**, *42*, 770–775. [CrossRef]
15. He, P.; Wang, Y.; Wang, X.; Pei, F.; Wang, H.; Liu, L.; Yi, L. Investigation of carbon supported Au–Ni bimetallic nanoparticles as electrocatalyst for direct borohydride fuel cell. *J. Power Sources* **2011**, *196*, 1042–1047. [CrossRef]
16. Liu, J.; Zhao, Q.; Wu, C.; Wang, Y.; Wei, W.; Wang, X.; Yi, L. Performance improvement of activated nanoporous carbon supported gold catalyst as an anode for direct borohydride–hydrogen peroxide fuel cells. *RSC Adv.* **2014**, *4*, 17129–17135. [CrossRef]
17. Yi, L.; Liu, L.; Wang, X.; Liu, X.; Yi, W.; Wang, X. Carbon supported Pt–Sn nanoparticles as anode catalyst for direct borohydride–hydrogen peroxide fuel cell: Electrocatalysis and fuel cell performance. *J. Power Sources* **2013**, *224*, 6–12. [CrossRef]
18. Oliveira, R.C.P.; Milikić, J.; Daş, E.; Yurtcan, A.B.; Santos, D.M.F.; Šljukić, B. Platinum/polypyrrole-carbon electrocatalysts for direct borohydride-peroxide fuel cells. *Appl. Catal. B Environ.* **2018**, *238*, 454–464. [CrossRef]
19. Freitas, K.S.; Concha, B.M.; Ticianelli, E.A.; Chatenet, M. Mass transport effects in the borohydride oxidation reaction—Influence of the residence time on the reaction onset and faradaic efficiency. *Catal. Today* **2011**, *170*, 110–119. [CrossRef]
20. Olu, P.-Y.; Barros, C.R.; Job, N.; Chatenet, M. Electrooxidation of NaBH4 in Alkaline Medium on Well-defined Pt Nanoparticles Deposited onto Flat Glassy Carbon Substrate: Evaluation of the Effects of Pt Nanoparticle Size, Inter-Particle Distance, and Loading. *Electrocatalysis* **2014**, *5*, 288–300. [CrossRef]
21. Šljukić, B.; Milikić, J.; Santos, D.M.F.; Sequeira, C.A.C.; Macciò, D.; Saccone, A. Electrocatalytic performance of Pt–Dy alloys for direct borohydride fuel cells. *J. Power Sources* **2014**, *272*, 335–343. [CrossRef]

22. Šljukić, B.; Milikić, J.; Santos, D.M.F.; Sequeira, C.A.C. Carbon-supported Pt0.75M0.25 (M=Ni or Co) electrocatalysts for borohydride oxidation. *Electrochim. Acta* **2013**, *107*, 577–583. [CrossRef]
23. Concha, B.M.; Chatenet, M. Direct oxidation of sodium borohydride on Pt, Ag and alloyed Pt–Ag electrodes in basic media. *Electrochim. Acta* **2009**, *54*, 6130–6139. [CrossRef]
24. Gyenge, E.; Atwan, M.; Northwood, D. Electrocatalysis of Borohydride Oxidation on Colloidal Pt and Pt-Alloys (Pt-Ir, Pt-Ni, and Pt-Au) and Application for Direct Borohydride Fuel Cell Anodes. *J. Electrochem. Soc.* **2006**, *153*, A150–A158. [CrossRef]
25. Santos, D.M.F.; Šljukić, B.; Amaral, L.; Macciò, D.; Saccone, A.; Sequeira, C.A.C. Nickel and Nickel-Cerium Alloy Anodes for Direct Borohydride Fuel Cells. *J. Electrochem. Soc.* **2014**, *161*, F594–F599. [CrossRef]
26. Hosseini, M.G.; Abdolmaleki, M.; Ashrafpoor, S. Electrocatalytic Oxidation of Sodium Borohydride on a Nanoporous Ni/Zn-Ni Electrode. *Chin. J. Catal.* **2012**, *33*, 1817–1824. [CrossRef]
27. Santos, D.M.F.; Sequeira, C.A.C. Zinc Anode for Direct Borohydride Fuel Cells. *J. Electrochem. Soc.* **2010**, *157*, B13–B19. [CrossRef]
28. Vinayan, B.P.; Jafri, R.I.; Nagar, R.; Rajalakshmi, N.; Sethupathi, K.; Ramaprabhu, S. Catalytic activity of platinum–cobalt alloy nanoparticles decorated functionalized multiwalled carbon nanotubes for oxygen reduction reaction in PEMFC. *Int. J. Hydrogen Energy* **2012**, *37*, 412–421. [CrossRef]
29. Rao, C.S.; Singh, D.; Sekhar, R.; Rangarajan, J. Pt–Co electrocatalyst with varying atomic percentage of transition metal. *Int. J. Hydrogen Energy* **2011**, *36*, 14805–14814. [CrossRef]
30. Tegou, A.; Papadimitriou, S.; Mintsouli, I.; Armyanov, S.; Valova, E.; Kokkinidis, G.; Sotiropoulos, S. Rotating disc electrode studies of borohydride oxidation at Pt and bimetallic Pt–Ni and Pt–Co electrodes. *Catal. Today* **2011**, *170*, 126–133. [CrossRef]
31. Šljukić, B.; Santos, D.M.F. Direct Borohydride Fuel Cells. In *Direct Liquid Fuel Cells: Fundamentals. Advances and Future*, 1st ed.; Akay, R.G., Yurtcan, A.B., Eds.; Academic Press: Cambridge, MA, USA, 2020; pp. 203–232. [CrossRef]
32. Chatenet, M.; Lima, F.H.B.; Ticianelli, E.A. Gold is not a Faradaic-Efficient Borohydride Oxidation Electrocatalyst: An Online Electrochemical Mass Spectrometry Study. *J. Electrochem. Soc.* **2010**, *157*, B697–B704. [CrossRef]
33. Braesch, G.; Bonnefont, A.; Martin, V.; Savinova, E.R.; Chatenet, M. Borohydride oxidation reaction mechanisms and poisoning effects on Au, Pt and Pd bulk electrodes: From model (low) to direct borohydride fuel cell operating (high) concentrations. *Electrochim. Acta* **2018**, *273*, 483–494. [CrossRef]
34. Tamašauskaitė-Tamašiūnaitė, L.; Radomskis, A.; Antanavičiūtė, K.; Jablonskienė, J.; Balciunaite, A.; Žielienė, A.; Naruškevičius, L.; Kondrotas, R.; Norkus, E. Graphene supported platinum–cobalt nanocomposites as electrocatalysts for borohydride oxidation. *Int. J. Hydrogen Energy* **2014**, *39*, 4282–4290. [CrossRef]
35. He, P.; Wang, X.; Liu, Y.; Liu, X.; Yi, L. Comparison of electrocatalytic activity of carbon-supported Au–M (M = Fe, Co, Ni, Cu and Zn) bimetallic nanoparticles for direct borohydride fuel cells. *Int. J. Hydrogen Energy* **2012**, *37*, 11984–11993. [CrossRef]
36. Modibedi, R.M.; Masombuka, T.; Mathe, M. Carbon supported Pd–Sn and Pd–Ru–Sn nanocatalysts for ethanol electro-oxidation in alkaline medium. *Int. J. Hydrogen Energy* **2011**, *36*, 4664–4672. [CrossRef]
37. Antolini, E. Palladium in fuel cell catalysis. *Energy Environ. Sci.* **2009**, *2*, 915–931. [CrossRef]
38. Huang, Y.; Guo, Y.; Wang, Y.; Yao, J. Synthesis and performance of a novel PdCuPb/C nanocatalyst for ethanol electrooxidation in alkaline medium. *Int. J. Hydrogen Energy* **2014**, *39*, 4274–4281. [CrossRef]
39. Zheng, Y.; Qiao, J.; Yuan, J.; Shen, J.; Wang, A.-J.; Huang, S. Controllable synthesis of PtPd nanocubes on graphene as advanced catalysts for ethanol oxidation. *Int. J. Hydrogen Energy* **2018**, *43*, 4902–4911. [CrossRef]
40. Yang, G.; Zhou, Y.; Pan, H.-B.; Zhu, C.; Fu, S.; Wai, C.M.; Du, D.; Zhu, J.-J.; Lin, Y. Ultrasonic-assisted synthesis of Pd–Pt/carbon nanotubes nanocomposites for enhanced electro-oxidation of ethanol and methanol in alkaline medium. *Ultrason. Sonochemistry* **2016**, *28*, 192–198. [CrossRef] [PubMed]
41. Brouzgou, A.; Podias, A.; Tsiakaras, P. PEMFCs and AEMFCs directly fed with ethanol: A current status comparative review. *J. Appl. Electrochem.* **2013**, *43*, 119–136. [CrossRef]
42. Santos, D.M.F.; Sequeira, C.A.C. Sodium borohydride determination by measurement of open circuit potentials. *J. Electroanal. Chem.* **2009**, *627*, 1–8. [CrossRef]
43. Hong, J.; Fang, B.; Wang, C.; Currie, K. Zn-Air Fuel Cell/Battery Hybrid Power Sources with Addition of Borohydride. *ECS Trans.* **2006**, *3*, 89–99. [CrossRef]
44. Hong, J.; Fang, B.; Wang, C.; Currie, K. Intrinsic borohydride fuel cell/battery hybrid power sources. *J. Power Sources* **2006**, *161*, 753–760. [CrossRef]
45. Wang, X.; Xia, Y. Electrocatalytic performance of PdCo–C catalyst for formic acid oxidation. *Electrochem. Commun.* **2008**, *10*, 1644–1646. [CrossRef]
46. Sheng, G.; Chen, J.; Ye, H.; Hu, Z.; Fu, X.-Z.; Sun, R.; Huang, W.; Wong, C.-P. Hollow PdCo alloy nanospheres with mesoporous shells as high-performance catalysts for methanol oxidation. *J. Colloid Interface Sci.* **2018**, *522*, 264–271. [CrossRef]
47. Martins, M.; Šljukić, B.; Metin, Ö.; Sevim, M.; Sequeira, C.A.C.; Şener, T.; Santos, D.M.F. Bimetallic PdM (M = Fe, Ag, Au) alloy nanoparticles assembled on reduced graphene oxide as catalysts for direct borohydride fuel cells. *J. Alloys Compd.* **2017**, *718*, 204–214. [CrossRef]
48. Martins, M.; Metin, Ö.; Sevim, M.; Šljukić, B.; Sequeira, C.A.C.; Sener, T.; Santos, D.M.F. Monodisperse Pd nanoparticles assembled on reduced graphene oxide-Fe_3O_4 nanocomposites as electrocatalysts for borohydride fuel cells. *Int. J. Hydrogen Energy* **2018**, *43*, 10686–10697. [CrossRef]

49. Simões, M.; Baranton, S.; Coutanceau, C. Electrooxidation of Sodium Borohydride at Pd, Au, and Pd_xAu_{1-x} Carbon-Supported Nanocatalysts. *J. Phys. Chem. C* **2009**, *113*, 13369–13376. [CrossRef]
50. Jimenez, I.M.; Janik, M.; De Leon, C.P.; Walsh, F. Pd–Ir alloy as an anode material for borohydride oxidation. *J. Power Sources* **2014**, *269*, 498–508. [CrossRef]
51. Grimmer, C.; Grandi, M.; Zacharias, R.; Cermenek, B.; Weber, H.; Morais, C.; Napporn, T.W.; Weinberger, S.; Schenk, A.; Hacker, V. The electrooxidation of borohydride: A mechanistic study on palladium (Pd/C) applying RRDE, 11B-NMR and FTIR. *Appl. Catal. B Environ.* **2016**, *180*, 614–621. [CrossRef]
52. Šljukić, B.; Martins, M.; Kayhan, E.; Balčiūnaitė, A.; Şener, T.; Sequeira, C.A.C.; Santos, D.M.F. SnO_2-C supported PdNi nanoparticles for oxygen reduction and borohydride oxidation. *J. Electroanal. Chem.* **2017**, *797*, 23–30. [CrossRef]
53. Milikić, J.; Ćirić-Marjanović, G.; Mentus, S.; Santos, D.M.F.; Sequeira, C.A.C.; Šljukić, B. Pd/c-PANI electrocatalysts for direct borohydride fuel cells. *Electrochim. Acta* **2016**, *213*, 298–305. [CrossRef]
54. Martins, M.; Šljukić, B.; Sequeira, C.A.C.; Metin, Ö.; Erdem, M.; Sener, T.; Santos, D.M.F. Biobased carbon-supported palladium electrocatalysts for borohydride fuel cells. *Int. J. Hydrogen Energy* **2016**, *41*, 10914–10922. [CrossRef]
55. Uosaki, K. *Electrochemical Science for a Sustainable Society: A Tribute to John O'M Bockris*, 1st ed.; Springer International Publishing: New York, NY, USA, 2017. [CrossRef]
56. Lv, H.; Sun, L.; Zou, L.; Xu, D.; Yao, H.; Liu, B. Size-dependent synthesis and catalytic activities of trimetallic PdAgCu mesoporous nanospheres in ethanol electrooxidation. *Chem. Sci.* **2019**, *10*, 1986–1993. [CrossRef] [PubMed]
57. Amin, R.; Hameed, R.A.; El-Khatib, K.; Youssef, M.E. Electrocatalytic activity of nanostructured Ni and Pd–Ni on Vulcan XC-72R carbon black for methanol oxidation in alkaline medium. *Int. J. Hydrogen Energy* **2014**, *39*, 2026–2041. [CrossRef]
58. Obradović, M.; Stančić, Z.; Lačnjevac, U.; Radmilovic, V.; Gavrilović-Wohlmuther, A.; Gojković, S. Electrochemical oxidation of ethanol on palladium-nickel nanocatalyst in alkaline media. *Appl. Catal. B Environ.* **2016**, *189*, 110–118. [CrossRef]
59. Dutta, A.; Datta, J. Energy efficient role of Ni/NiO in PdNi nano catalyst used in alkaline DEFC. *J. Mater. Chem. A* **2014**, *2*, 3237–3250. [CrossRef]
60. Shen, S.; Zhao, T.S.; Xu, J.; Li, Y. High performance of a carbon supported ternary PdIrNi catalyst for ethanol electro-oxidation in anion-exchange membrane direct ethanol fuel cells. *Energy Environ. Sci.* **2011**, *4*, 1428–1433. [CrossRef]
61. Yurderi, M.; Bulut, A.; Zahmakiran, M.; Kaya, M. Carbon supported trimetallic PdNiAg nanoparticles as highly active, selective and reusable catalyst in the formic acid decomposition. *Appl. Catal. B Environ.* **2014**, *160*, 514–524. [CrossRef]
62. Zhu, W.; Ke, J.; Wang, S.-B.; Ren, J.; Wang, H.-H.; Zhou, Z.-Y.; Si, R.; Zhang, Y.-W.; Yan, C.-H. Shaping Single-Crystalline Trimetallic Pt–Pd–Rh Nanocrystals toward High-Efficiency C–C Splitting of Ethanol in Conversion to CO_2. *ACS Catal.* **2015**, *5*, 1995–2008. [CrossRef]
63. Hu, S.; Munoz, F.; Noborikawa, J.; Haan, J.; Scudiero, L.; Ha, S. Carbon supported Pd-based bimetallic and trimetallic catalyst for formic acid electrochemical oxidation. *Appl. Catal. B Environ.* **2016**, *180*, 758–765. [CrossRef]
64. Sharma, G.; Kumar, D.; Kumar, A.; Al-Muhtaseb, A.H.; Pathania, D.; Naushad, M.; Mola, G.T. Revolution from monometallic to trimetallic nanoparticle composites, various synthesis methods and their applications: A review. *Mater. Sci. Eng. C* **2017**, *71*, 1216–1230. [CrossRef]
65. Ulas, B.; Caglar, A.; Sahin, O.; Kivrak, H. Composition dependent activity of PdAgNi alloy catalysts for formic acid electrooxidation. *J. Colloid Interface Sci.* **2018**, *532*, 47–57. [CrossRef]
66. Beyhan, S.; Léger, J.-M.; Kadırgan, F. Understanding the influence of Ni, Co, Rh and Pd addition to PtSn/C catalyst for the oxidation of ethanol by in situ Fourier transform infrared spectroscopy. *Appl. Catal. B Environ.* **2014**, *144*, 66–74. [CrossRef]
67. Shang, C.; Hong, W.; Wang, J.; Wang, E. Carbon supported trimetallic nickel–palladium–gold hollow nanoparticles with superior catalytic activity for methanol electrooxidation. *J. Power Sources* **2015**, *285*, 12–15. [CrossRef]
68. Dutta, A.; Datta, J. Outstanding Catalyst Performance of PdAuNi Nanoparticles for the Anodic Reaction in an Alkaline Direct Ethanol (with Anion-Exchange Membrane) Fuel Cell. *J. Phys. Chem. C* **2012**, *116*, 25677–25688. [CrossRef]
69. Su, P.-C.; Chen, H.-S.; Chen, T.-Y.; Liu, C.-W.; Lee, C.-H.; Lee, J.-F.; Chan, T.-S.; Wang, K.-W. Enhancement of electrochemical properties of Pd/C catalysts toward ethanol oxidation reaction in alkaline solution through Ni and Au alloying. *Int. J. Hydrogen Energy* **2013**, *38*, 4474–4482. [CrossRef]
70. Lu, L.; Kang, J. Amperometric nonenzymatic sensing of glucose at very low working potential by using a nanoporous PdAuNi ternary alloy. *Microchim. Acta* **2018**, *185*, 111. [CrossRef] [PubMed]
71. Bulut, A.; Yurderi, M.; Kaya, M.; Aydemir, M.; Baysal, A.; Durap, F.; Zahmakiran, M. Amine-functionalized graphene nanosheet-supported PdAuNi alloy nanoparticles: Efficient nanocatalyst for formic acid dehydrogenation. *New J. Chem.* **2018**, *42*, 16103–16114. [CrossRef]
72. Li, S.; Lai, J.; Luque, R.; Xu, G. Designed multimetallic Pd nanosponges with enhanced electrocatalytic activity for ethylene glycol and glycerol oxidation. *Energy Environ. Sci.* **2016**, *9*, 3097–3102. [CrossRef]
73. Chatenet, M.; Molina-Concha, M.; Diard, J.-P. First insights into the borohydride oxidation reaction mechanism on gold by electrochemical impedance spectroscopy. *Electrochim. Acta* **2009**, *54*, 1687–1693. [CrossRef]
74. Nagle, L.C.; Rohan, J. Nanoporous gold anode catalyst for direct borohydride fuel cell. *Int. J. Hydrogen Energy* **2011**, *36*, 10319–10326. [CrossRef]

75. Tegou, A.; Armyanov, S.; Valova, E.; Steenhaut, O.; Hubin, A.; Kokkinidis, G.; Sotiropoulos, S. Mixed platinum–gold electrocatalysts for borohydride oxidation prepared by the galvanic replacement of nickel deposits. *J. Electroanal. Chem.* **2009**, *634*, 104–110. [CrossRef]
76. Parrour, G.; Chatenet, M.; Diard, J.-P. Electrochemical impedance spectroscopy study of borohydride oxidation reaction on gold—Towards a mechanism with two electrochemical steps. *Electrochim. Acta* **2010**, *55*, 9113–9124. [CrossRef]
77. Santos, D.M.F.; Sequeira, C.A.C. Chronopotentiometric Investigation of Borohydride Oxidation at a Gold Electrode. *J. Electrochem. Soc.* **2010**, *157*, F16–F21. [CrossRef]
78. Zhang, D.; Cheng, K.; Shi, N.; Guo, F.; Wang, G.; Cao, D. Nickel particles supported on multi-walled carbon nanotubes modified sponge for sodium borohydride electrooxidation. *Electrochem. Commun.* **2013**, *35*, 128–130. [CrossRef]
79. Santos, D.M.F.; Šljukić, B.; Amaral, L.; Milikić, J.; Sequeira, C.A.C.; Macciò, D.; Saccone, A. Nickel–rare earth electrodes for sodium borohydride electrooxidation. *Electrochim. Acta* **2016**, *190*, 1050–1056. [CrossRef]
80. Oshchepkov, A.G.; Braesch, G.; Ould-Amara, S.; Rostamikia, G.; Maranzana, G.; Bonnefont, A.; Papaefthimiou, V.; Janik, M.J.; Chatenet, M.; Savinova, E.R. Nickel Metal Nanoparticles as Anode Electrocatalysts for Highly Efficient Direct Borohydride Fuel Cells. *ACS Catal.* **2019**, *9*, 8520–8528. [CrossRef]
81. Chen, A.; Ostrom, C. Palladium-Based Nanomaterials: Synthesis and Electrochemical Applications. *Chem. Rev.* **2015**, *115*, 11999–12044. [CrossRef]
82. Zhang, Z.; Dong, Y.; Wang, L.; Wang, S. Scalable synthesis of a Pd nanoparticle loaded hierarchically porous graphene network through multiple synergistic interactions. *Chem. Commun.* **2015**, *51*, 8357–8360. [CrossRef] [PubMed]
83. Corradini, P.G.; Pires, F.I.; Paganin, V.A.; Perez, J.; Antolini, E. Effect of the relationship between particle size, inter-particle distance, and metal loading of carbon supported fuel cell catalysts on their catalytic activity. *J. Nanoparticle Res.* **2012**, *14*, 1–9. [CrossRef]
84. Modibedi, R.M.; Mehlo, T.; Ozoemena, K.I.; Mathe, M. Preparation, characterisation and application of Pd/C nanocatalyst in passive alkaline direct ethanol fuel cells (ADEFC). *Int. J. Hydrogen Energy* **2015**, *40*, 15605–15612. [CrossRef]
85. Kim, P.; Joo, J.B.; Kim, W.; Kim, J.; Song, I.K.; Yi, J. NaBH4-assisted ethylene glycol reduction for preparation of carbon-supported Pt catalyst for methanol electro-oxidation. *J. Power Sources* **2006**, *160*, 987–990. [CrossRef]
86. Henrique, R.S.; Ayoub, J.M.S.; Piasentin, R.M.; Linardi, M.; Santos, M.C. Preparation of Pt/C-In_2O_3.SnO_2 electrocatalysts by borohydride reduction process for ethanol electro-oxidation. *Int. J. Electrochem. Sci.* **2012**, *7*, 2036–2046. [CrossRef]
87. Assumpção, M.; da Silva, S.; De Souza, R.; Buzzo, G.; Spinacé, E.; Santos, M.; Neto, A.; Silva, J. Investigation of PdIr/C electrocatalysts as anode on the performance of direct ammonia fuel cell. *J. Power Sources* **2014**, *268*, 129–136. [CrossRef]
88. Miller, S.D.; İnoğlu, N.; Kitchin, J. Configurational correlations in the coverage dependent adsorption energies of oxygen atoms on late transition metal fcc(111) surfaces. *J. Chem. Phys.* **2011**, *134*, 104709. [CrossRef]
89. Counsell, J.D.P. Surface Science Studies of Adsorption and Reactivity of Pd (111) and Au-Pd (111). Ph.D. Thesis, Cardiff University, Cardiff, Wales, UK, 2010.
90. Naresh, N.; Wasim, F.G.S.; Ladewig, B.P.; Neergat, M. Removal of surfactant and capping agent from Pd nanocubes (Pd-NCs) using tert-butylamine: Its effect on electrochemical characteristics. *J. Mater. Chem. A* **2013**, *1*, 8553–8559. [CrossRef]
91. Zhang, X.-J.; Zhang, J.-M.; Zhang, P.-Y.; Li, Y.; Xiang, S.; Tang, H.-G.; Fan, Y.-J. Highly active carbon nanotube-supported Ru@Pd core-shell nanostructure as an efficient electrocatalyst toward ethanol and formic acid oxidation. *Mol. Catal.* **2017**, *436*, 138–144. [CrossRef]
92. Qiu, X.; Dai, Y.; Tang, Y.; Lu, T.; Wei, S.; Chen, Y. One-pot synthesis of gold–palladium@palladium core–shell nanoflowers as efficient electrocatalyst for ethanol electrooxidation. *J. Power Sources* **2015**, *278*, 430–435. [CrossRef]
93. Zhou, W.; Lee, J.Y. Highly active core–shell Au@Pd catalyst for formic acid electrooxidation. *Electrochem. Commun.* **2007**, *9*, 1725–1729. [CrossRef]
94. Akhairi, M.; Kamarudin, S. Catalysts in direct ethanol fuel cell (DEFC): An overview. *Int. J. Hydrogen Energy* **2016**, *41*, 4214–4228. [CrossRef]
95. Feng, Y.-Y.; Liu, Z.-H.; Xu, Y.; Wang, P.; Wang, W.-H.; Kong, D.-S. Highly active PdAu alloy catalysts for ethanol electro-oxidation. *J. Power Sources* **2013**, *232*, 99–105. [CrossRef]
96. Feng, Y.; Bin, D.; Yan, B.; Du, Y.; Majima, T.; Zhou, W. Porous bimetallic PdNi catalyst with high electrocatalytic activity for ethanol electrooxidation. *J. Colloid Interface Sci.* **2017**, *493*, 190–197. [CrossRef]
97. Akhtar, K.; Khan, S.A.; Khan, S.B.; Asiri, A.M. Scanning Electron Microscopy: Principle and Applications in Nanomaterials Characterization. In *Handbook of Materials Characterization*; Akhtar, K., Khan, S.A., Khan, S.B., Asiri, A.M., Eds.; Springer International Publishing: Bassel, Switzerland, 2018; pp. 113–145. [CrossRef]
98. Pasqualeti, A.M.; Olu, P.-Y.; Chatenet, M.; Lima, F.H.B. Borohydride Electrooxidation on Carbon-Supported Noble Metal Nanoparticles: Insights into Hydrogen and Hydroxyborane Formation. *ACS Catal.* **2015**, *5*, 2778–2787. [CrossRef]
99. Santos, D.M.F.; Saturnino, P.; Lobo, R.F.M.; Sequeira, C.A.C. Direct borohydride/peroxide fuel cells using Prussian Blue cathodes. *J. Power Sources* **2012**, *208*, 131–137. [CrossRef]
100. Santos, D.M.F.; Sequeira, C.A.C. Effect of Membrane Separators on the Performance of Direct Borohydride Fuel Cells. *J. Electrochem. Soc.* **2011**, *159*, B126–B132. [CrossRef]
101. Lam, B.T.X.; Chiku, M.; Higuchi, E.; Inoue, H. Preparation of PdAg and PdAu nanoparticle-loaded carbon black catalysts and their electrocatalytic activity for the glycerol oxidation reaction in alkaline medium. *J. Power Sources* **2015**, *297*, 149–157. [CrossRef]

102. Zhang, S.; Qing, M.; Zhang, H.; Tian, Y. Electrocatalytic oxidation of formic acid on functional MWCNTs supported nanostructured Pd–Au catalyst. *Electrochem. Commun.* **2009**, *11*, 2249–2252. [CrossRef]
103. Liu, C.; Liu, R.-H.; Sun, Q.-J.; Chang, J.-B.; Gao, X.; Liu, Y.; Lee, S.-T.; Kang, Z.-H.; Wang, S.-D. Controlled synthesis and synergistic effects of graphene-supported PdAu bimetallic nanoparticles with tunable catalytic properties. *Nanoscale* **2015**, *7*, 6356–6362. [CrossRef]
104. Geraldes, A.N.; da Silva, D.F.; Pino, E.S.; da Silva, J.C.M.; de Souza, R.F.B.; Hammer, P.; Spinacé, E.V.; Neto, A.O.; Linardi, M.; dos Santos, M.C. Ethanol electro-oxidation in an alkaline medium using Pd/C, Au/C and PdAu/C electrocatalysts prepared by electron beam irradiation. *Electrochim. Acta* **2013**, *111*, 455–465. [CrossRef]
105. Zhang, G.; Wang, Y.; Wang, X.; Chen, Y.; Zhou, Y.; Tang, Y.; Lu, L.; Bao, J.; Lu, T. Preparation of Pd–Au/C catalysts with different alloying degree and their electrocatalytic performance for formic acid oxidation. *Appl. Catal. B Environ.* **2011**, *102*, 614–619. [CrossRef]
106. Dutta, A.; Mondal, A.; Broekmann, P.; Datta, J. Optimal level of Au nanoparticles on Pd nanostructures providing remarkable electro-catalysis in direct ethanol fuel cell. *J. Power Sources* **2017**, *361*, 276–284. [CrossRef]
107. Qin, Y.-H.; Jiang, Y.; Niu, D.-F.; Zhang, X.-S.; Zhou, X.-G.; Niu, L.; Yuan, W.-K. Carbon nanofiber supported bimetallic PdAu nanoparticles for formic acid electrooxidation. *J. Power Sources* **2012**, *215*, 130–134. [CrossRef]
108. Yin, Z.; Chi, M.; Zhu, Q.; Ma, D.; Sun, J.; Bao, X. Supported bimetallic PdAu nanoparticles with superior electrocatalytic activity towards methanol oxidation. *J. Mater. Chem. A* **2013**, *1*, 9157–9163. [CrossRef]
109. Zhang, Z.; Xin, L.; Sun, K.; Li, W. Pd–Ni electrocatalysts for efficient ethanol oxidation reaction in alkaline electrolyte. *Int. J. Hydrogen Energy* **2011**, *36*, 12686–12697. [CrossRef]
110. Holade, Y.; Sahin, N.E.; Servat, K.; Napporn, T.W.; Kokoh, K.B. Recent Advances in Carbon Supported Metal Nanoparticles Preparation for Oxygen Reduction Reaction in Low Temperature Fuel Cells. *Catalysts* **2015**, *5*, 310–348. [CrossRef]
111. Zhu, C.; Wen, D.; Oschatz, M.; Holzschuh, M.; Liu, W.; Herrmann, A.-K.; Simon, F.; Kaskel, S.; Eychmüller, A. Kinetically Controlled Synthesis of PdNi Bimetallic Porous Nanostructures with Enhanced Electrocatalytic Activity. *Small* **2015**, *11*, 1430–1434. [CrossRef] [PubMed]
112. Chen, W.; Zhang, Y.; Wei, X. Catalytic performances of PdNi/MWCNT for electrooxidations of methanol and ethanol in alkaline media. *Int. J. Hydrogen Energy* **2015**, *40*, 1154–1162. [CrossRef]
113. Ramulifho, T.; Ozoemena, K.I.; Modibedi, R.M.; Jafta, C.J.; Mathe, M. Electrocatalytic oxidation of ethylene glycol at palladium-bimetallic nanocatalysts (PdSn and PdNi) supported on sulfonate-functionalised multi-walled carbon nanotubes. *J. Electroanal. Chem.* **2013**, *692*, 26–30. [CrossRef]
114. Chen, L.Y.; Chen, N.; Hou, Y.; Wang, Z.C.; Lv, S.H.; Fujita, T.; Jiang, J.H.; Hirata, A.; Chen, M. Geometrically Controlled Nanoporous PdAu Bimetallic Catalysts with Tunable Pd/Au Ratio for Direct Ethanol Fuel Cells. *ACS Catal.* **2013**, *3*, 1220–1230. [CrossRef]
115. Behmenyar, G.; Akın, A.N. Investigation of carbon supported Pd–Cu nanoparticles as anode catalysts for direct borohydride fuel cell. *J. Power Sources* **2014**, *249*, 239–246. [CrossRef]
116. Park, S.Y.; Lee, D.-W.; Park, I.S.; Hong, Y.-K.; Park, Y.-M.; Lee, K.-Y. The effective bimetallic component of Pd–Au/C for electrochemical oxidation of borohydrides. *Curr. Appl. Phys.* **2010**, *10*, S40–S43. [CrossRef]
117. He, P.; Wang, X.; Liu, Y.; Yi, L.; Liu, X. Reverse micelle synthesis of AuNi alloy as electrocatalyst of borohydride oxidation. *Int. J. Hydrogen Energy* **2012**, *37*, 1254–1262. [CrossRef]
118. Yang, J.Q.; Liu, B.H.; Wu, S. Carbon-supported Pd catalysts: Influences of nanostructure on their catalytic performances for borohydride electrochemical oxidation. *J. Power Sources* **2009**, *194*, 824–829. [CrossRef]
119. Duan, D.; Yin, X.; Wang, Q.; Liu, S.; Wang, Y. Performance evaluation of borohydride electrooxidation reaction with ternary alloy Au–Ni–Cu/C catalysts. *J. Appl. Electrochem.* **2018**, *48*, 835–847. [CrossRef]
120. Antolini, E. Structural parameters of supported fuel cell catalysts: The effect of particle size, inter-particle distance and metal loading on catalytic activity and fuel cell performance. *Appl. Catal. B Environ.* **2016**, *181*, 298–313. [CrossRef]
121. Bard, A.J.; Faulkner, L.R. *Electrochemical Methods: Fundamentals and Applications*, 2nd ed.; John Wiley & Sons, Inc.: New York, NY, USA, 2001. [CrossRef]
122. Wei, J.; Wang, X.; Wang, Y.; Chen, Q.; Pei, F.; Wang, Y. Investigation of carbon-supported Au hollow nanospheres as electrocatalyst for electrooxidation of sodium borohydride. *Int. J. Hydrogen Energy* **2009**, *34*, 3360–3366. [CrossRef]
123. Wang, K.; Lu, J.; Zhuang, L. A Current−Decomposition Study of the Borohydride Oxidation Reaction at Ni Electrodes. *J. Phys. Chem. C* **2007**, *111*, 7456–7462. [CrossRef]
124. Hosseini, M.G.; Abdolmaleki, M. Synthesis and characterization of porous nanostructured Ni/PdNi electrode towards electrooxidation of borohydride. *Int. J. Hydrogen Energy* **2013**, *38*, 5449–5456. [CrossRef]
125. Oliveira, R.C.P.; Vasić, M.; Santos, D.M.F.; Babić, B.; Hercigonja, R.; Sequeira, C.A.C.; Šljukić, B. Performance assessment of a direct borohydride-peroxide fuel cell with Pd-impregnated faujasite X zeolite as anode electrocatalyst. *Electrochim. Acta* **2018**, *269*, 517–525. [CrossRef]
126. Yi, L.; Song, Y.; Wang, X.; Yi, L.; Hu, J.; Su, G.; Yi, W.; Yan, H. Carbon supported palladium hollow nanospheres as anode catalysts for direct borohydride-hydrogen peroxide fuel cells. *J. Power Sources* **2012**, *205*, 63–70. [CrossRef]

127. Song, C.; Wang, G.; Li, B.; Miao, C.; Ma, K.; Zhu, K.; Cheng, K.; Ye, K.; Yan, J.; Cao, D.; et al. A novel electrode of ternary CuNiPd nanoneedles decorated Ni foam and its catalytic activity toward $NaBH_4$ electrooxidation. *Electrochim. Acta* **2019**, *299*, 395–404. [CrossRef]
128. Oh, T.H.; Jang, B.; Kwon, S. Performance evaluation of direct borohydride–hydrogen peroxide fuel cells with electrocatalysts supported on multiwalled carbon nanotubes. *Energy* **2014**, *76*, 911–919. [CrossRef]
129. Pei, F.; Wang, Y.; Wang, X.; He, P.; Chen, Q.; Wang, X.; Wang, H.; Yi, L.; Guo, J. Performance of supported Au–Co alloy as the anode catalyst of direct borohydride-hydrogen peroxide fuel cell. *Int. J. Hydrogen Energy* **2010**, *35*, 8136–8142. [CrossRef]
130. Mahmoodi, R.; Hosseini, M.G.; Rasouli, H. Enhancement of output power density and performance of direct borohydride-hydrogen peroxide fuel cell using Ni-Pd core-shell nanoparticles on polymeric composite supports (rGO-PANI) as novel electrocatalysts. *Appl. Catal. B Environ.* **2019**, *251*, 37–48. [CrossRef]
131. Hosseini, M.; Mahmoodi, R.; Amjadi, M.S. Carbon supported Ni_1Pt_1 nanocatalyst as superior electrocatalyst with increased power density in direct borohydride-hydrogen peroxide and investigation of cell impedance at different temperatures and discharging currents. *Energy* **2017**, *131*, 137–148. [CrossRef]